Quantum computation of a complex system: The kicked Harper model

B. Lévi and B. Georgeot
Laboratoire de Physique Théorique, UMR 5152 du CNRS, Université Paul Sabatier, F-31062 Toulouse Cedex 4, France
(Received 11 June 2004; published 22 November 2004)

The simulation of complex quantum systems on a quantum computer is studied, taking the kicked Harper model as an example. This well-studied system has a rich variety of dynamical behavior depending on parameters, displays interesting phenomena such as fractal spectra, mixed phase space, dynamical localization, anomalous diffusion, or partial delocalization, and can describe electrons in a magnetic field. Three different quantum algorithms are presented and analyzed, enabling us to simulate efficiently the evolution operator of this system with different precision using different resources. Depending on the parameters chosen, the system is near integrable, localized, or partially delocalized. In each case we identify transport or spectral quantities which can be obtained more efficiently on a quantum computer than on a classical one. In most cases, a polynomial gain compared to classical algorithms is obtained, which can be quadratic or less depending on the parameter regime. We also present the effects of static imperfections on the quantities selected and show that depending on the regime of parameters, very different behaviors are observed. Some quantities can be obtained reliably with moderate levels of imperfection even for large number of qubits, whereas others are exponentially sensitive to the number of qubits. In particular, the imperfection threshold for delocalization becomes exponentially small in the partially delocalized regime. Our results show that interesting behavior can be observed with as little as 7–8 qubits and can be reliably measured in presence of moderate levels of internal imperfections.

DOI: 10.1103/PhysRevE.70.056218 PACS number(s): 05.45.Mt, 03.67.Lx, 72.15.Rn

I. INTRODUCTION

In the past few years, the field of quantum information [1] has attracted more and more attention in the scientific community. Among the most fascinating promises of this domain is the possibility of building a quantum computer. Such a quantum processor can use the superposition principle and the interferences of quantum mechanics to perform new types of algorithms which can be much more efficient than classical algorithms. Celebrated examples are Shor's algorithm which factors large integers exponentially faster than any known classical algorithm [2] and Grover's algorithm which searches unstructured lists quadratically faster than classical methods [3]. Another type of quantum algorithms concerns the simulation of physical systems. Examples include many-body quantum systems [4], classical and quantum spin systems [5], and classical dynamical systems [6,7]. Algorithms implementing quantum maps are especially interesting, since the systems simulated have simple equations of motion but can display very complex behaviors. Their simplicity enables one to simulate them with a small number of qubits. For example, it is possible to simulate efficiently the baker map [8] (experimental implementation with the NMR technique has already been performed [9]), the quantum kicked rotator [10,11], the sawtooth map [12], or the tent map [13]. In such algorithms, it is important to determine which physical quantities can be obtained accurately through measurement on the quantum computer and what is the total algorithmic complexity of the whole process. It is equally important to determine the effects of errors in the computation to assess the efficiency of the algorithm on a realistic quantum computer.

In the present paper, we will study in detail an important example of quantum map—namely, the kicked Harper model. The Hamiltonian of this system has a simple form, yet displays many interesting physical features not present in quantum maps previously studied in this context, such as fractal spectra, stochastic web, anomalous diffusion, or coexistence of localized and delocalized states. It was introduced in the context of solid-state physics (motion of electrons in presence of magnetic field) and has been the subject of many studies. Using this model as a test ground, we will present three different ways of simulating the quantum map on a quantum computer, two of them inspired by previous works, and compare their efficiency. We will then present examples of physical quantities which can be obtained on a quantum computer. It turns out that depending on the parameters of the system, at least polynomial speedup compared to classical algorithms can be obtained for different quantities. Numerical simulations and analytical estimations will also evaluate the effects of imperfections in the quantum computer on the estimation of these quantities.

II. HARPER AND KICKED HARPER MODELS

The Harper model was introduced in 1955 [14] to describe the motion of electrons in a two-dimensional lattice in presence of a magnetic field. Its Hamiltonian reads

$$H_0(I,\theta) = \cos(I) + \cos(\theta). \tag{1}$$

This Hamiltonian has been the subject of many studies (see, for example, [15–19]), but its dynamics is somewhat restricted by the fact that it describes an integrable system. A generalization of this model was introduced some time ago; it is called the kicked Harper model:

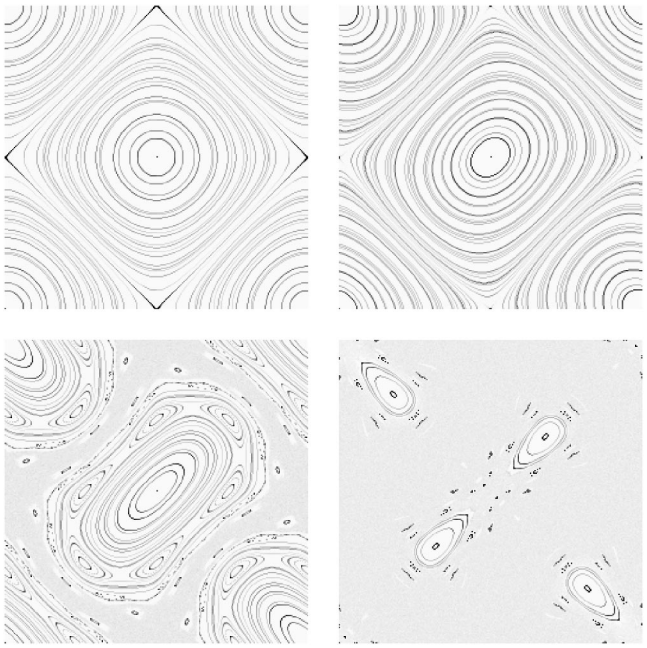

FIG. 1. Phase space of the classical kicked Harper model: $K=L\to 0$ (Harper model) (upper left), $K=L=0.5$ (upper right), $K=L=1.5$ (lower left), and $K=L=2.5$ (lower right) (10 000 iterations of 256 classical orbits). One cell of size $2\pi\times 2\pi$ is shown, the phase space being periodic.

$$H(I,\theta,t) = L\cos(I) + K\cos(\theta)\sum_m \delta(t-m), \tag{2}$$

where m runs through all integers values and K,L are constants. This Hamiltonian reduces to Eq. (1) in the limit $K=L\to 0$, but has a more complex dynamics depending on the parameters. Its dynamics between two kicks can be integrated to yield the map

$$\overline{I} = I + K\sin\theta, \quad \overline{\theta} = \theta - L\sin\overline{I}. \tag{3}$$

As in the case of the kicked rotator, there is a classical periodicity in both θ and I. Thus the phase space is composed of cells of size $2\pi\times 2\pi$ where the same structures repeat themselves.

This map (3) has been related to the motion of electrons in a perpendicular magnetic and electric fields and also to the problem of stochastic heating of a plasma in a magnetic field.

The quantization of Eq. (2) yields a periodic Hamiltonian which after integration over one period yields a unitary evolution operator acting on the wave function ψ:

$$\overline{\psi} = \hat{U}\psi = e^{-iL\cos(\hbar\hat{n})/\hbar}e^{-iK\cos(\hat{\theta})/\hbar}\psi, \tag{4}$$

where $\hat{n}=-iQ\partial/\partial\theta$ and $\psi(\theta+2Q\pi)=\psi(\theta)$.

This system has been the subject of many studies in the past few years, which focused on localization properties [20–27], tunneling properties [28,29], etc.

In the limit $K=L\to 0$ the system is classically integrable. For small K,L, chaos begins to appear around separatrices and spreads over larger and larger phase space areas as K,L increase (see Fig. 1). In the regime of small K,L, classical transport from cell to cell is possible only in the very small chaotic zones around separatrices. For $K=L$, this network of thin chaotic zones surrounding large islands is called the "stochastic web" (see Fig. 2). For intermediate values of K,L, the phase space is mixed, with integrable islands separated by large chaotic zones. For larger K,L, classical chaos is present in most of the phase space (cf. Fig. 1), and a typical trajectory will diffuse through the system. The quantum dynamics is related to these classical properties, but shows some striking differences. In the limit $K=L\to 0$, the system is integrable and wave functions are concentrated around classical tori, but complexity manifests itself in the spectrum of the Hamiltonian, which is fractal ("Hofstadter butterfly"). For small K,L the motion of a quantum wave packet is dominated by the presence of classical invariant curves; the wave packet can spread in between these curves or cross them by quantum tunneling. For larger K,L, in the regime of classical diffusion, as in the kicked rotator, a phenomenon similar to Anderson localization of electrons in disordered solids takes place. Through this phenomenon, called dynamical localization, a wave packet started at some value of momentum n will first spread, but contrary to classical trajectories this spreading will saturate. This corresponds to the fact that eigenfunctions $\psi_a(n)$ of $\hat{U}$ in Eq. (4) in momentum space (they are called Floquet eigenfunctions since they correspond to the action of the evolution operator during one period) are exponentially localized. Their envelopes obey the law $\psi_a(n)\sim\exp(-|n-m|/l)/\sqrt{l}$ where m marks the center of the eigenstate and l is the localization length. This phenomenon is especially visible for moderate values of K, where all eigenfunctions are localized. For larger values of K, the system undergoes a transition: some eigenfunctions are still localized, but more and more are delocalized (ergodic) and spread over the whole system. This coexistence of localized and delocalized states gives rise to specific physical properties. Indeed, it is very different from what happens in the

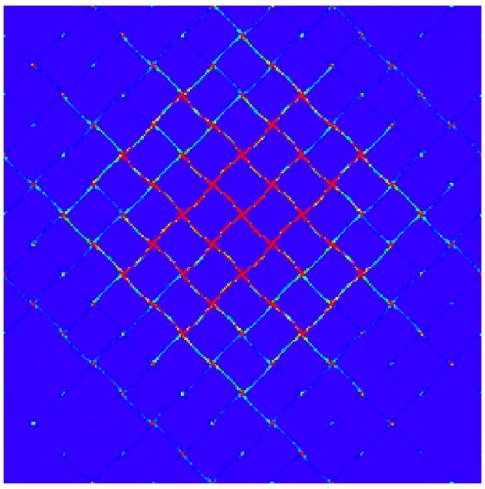

FIG. 2. (Color online) Example of stochastic web in the kicked Harper model. Here $K=L=0.5$, phase space is 8×8 cells of size $2\pi\times 2\pi$, and the figure shows positions after $t=1000$ iterations of 10^6 classical trajectories initially distributed according to a Gaussian centered half a cell above the center with standard deviation $\sqrt{2\pi/2^{25}}\approx 0.0004$. Color (grayness) shows the density of points, from red (gray) (maximal value) to blue (black) (minimal value).

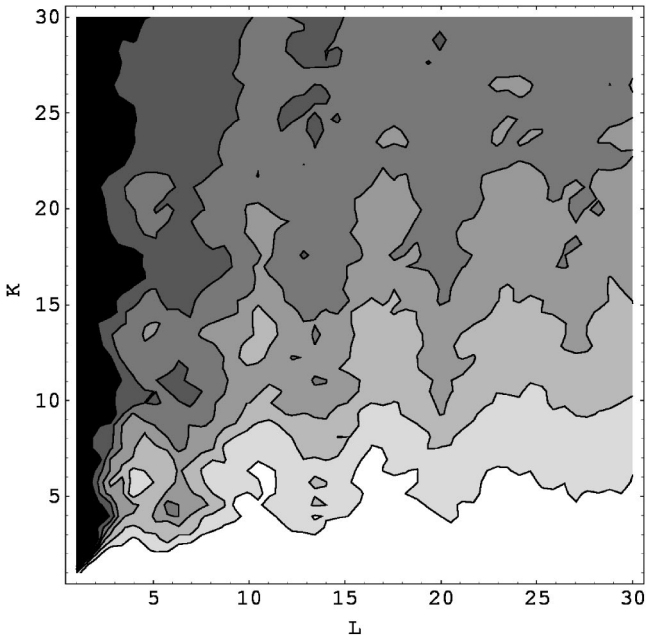

FIG. 3. Map of delocalization in the (K,L) plane. Grayness represents the inverse participation ratio $\xi=1/\Sigma_n|\psi(n)|^4$ (IPR), a measure of delocalization of states, from $\xi=1$ (state localized on one momentum state) to $\xi=N_H$ (totally delocalized state) (N_H is the dimension of the Hilbert space). Contour lines correspond to values of ξ ranging from 32 to 192 by increments of 32, $N_H=2^9$, $\hbar/2\pi=(13-\sqrt{5})/82$ (actual value is the nearest fraction with denominator 2^9). White corresponds to lowest values, black to maximal values of ξ. Each ξ value is obtained by averaging over all eigenstates of the evolution operator $\hat{U}$ of Eq. (4).

kicked rotator model, where usually all states are localized once classical chaos is present (see, for example, [11]) or in the Anderson transition (investigated in [30]) where the transition separates a regime where all eigenstates are localized from a regime where all are delocalized. In this regime of partial delocalization, an initial wave packet will spread, but a certain fraction of the total probability will remain localized. In addition, the diffusion of probability in momentum space has been shown numerically to be anomalous, with an exponent depending on the parameter values [17,22,23]. These properties are summarized by the phase diagram of Fig. 3. Different quantities can be obtained in these different regimes with the help of a quantum computer.

The phase space can be decomposed in cells of size $2\pi\times 2\pi$. Its global topology depends on boundary conditions. For a system of size N_H, if the phase space is closed with periodic boundary conditions, with, respectively, Q and P cells in the θ and n directions, then $\hbar=2\pi PQ/N_H$. Therefore, if one wants to keep $\hbar$ constant, the product PQ should be chosen such that PQ/N_H is the closest rational to $\hbar/(2\pi)$. For most of the results of this paper, the phase space will be a cylinder closed in the θ direction ($Q=1$) and extended in the direction of momentum, and transport properties will be studied in the momentum direction, as in the kicked rotator. In this case $\hbar/(2\pi)$ was set to $1/\{6+1/[(\sqrt{5}-1)/2]\}=(13-\sqrt{5})/82$ as in [23] to avoid unwanted arithmetical effects. The choice of a constant $\hbar$ implies that changing the number of qubits leads to increasing the size of phase space (number of cells) in the n direction. Only for the study of the stochastic web present at small $K=L$ (Sec. IV A) will the phase space be extended in both directions and its size (number of cells) fixed. In this case increasing the number of qubits leads to smaller and smaller $\hbar$.

III. SIMULATING THE TIME EVOLUTION: THREE POSSIBLE ALGORITHMS

The evolution operator (4) is composed of two transformations which are diagonal in, respectively, the momentum and position representations. This form is general for a family of kicked maps such as the kicked rotator, sawtooth map, and others. On a classical computer, the fastest way to implement such an evolution operator on a wave function of N_H components is to use the fast Fourier transform (FFT) algorithm to shift back and forth between the n and θ representations and to implement each operator by direct multiplication in the basis where it is diagonal. In this way, $O(N_H \log N_H)$ classical operations are needed to implement Eq. (4) on a N_H-dimensional vector. On a quantum computer, it is possible to use the quantum Fourier transform (QFT) to shift between momentum and position representations, using $O((\log N_H)^2)$ quantum gates. In each representation, one has then to implement the multiplication by a phase, $e^{-iL\cos(\hbar\hat{n})/\hbar}$ and $e^{-iK\cos(\hat{\theta})/\hbar}$.

In the following we will envision three different strategies to implement these diagonal operators: (i) exact computation using additional registers to hold the values of the cosines, (ii) decomposition into a sequence of simpler operators which are good approximations during short time slices, and (iii) direct computation, the cosine function being approximated by a (Chebyshev) polynomial.

The first one is in principle exact, but requires extra registers, and was already proposed in [10]. The second one has some similarities with the one explained in [30] for another system. The third one was not used in the context of quantum algorithms to the best of our knowledge, although the method is well known in computer science (see, for example, [31] for a recent use of this method to simulate many-spin systems on a classical computer). We note that an approximate algorithm to simulate the kicked Harper for long time was used in [32]; however, in that paper the aim of the authors was different, since they only wanted to construct efficiently a good approximation of the ground-state wave function in order to use it for generating phase-space distributions of other systems, and it is not clear that the method works for other purposes. We also note that the simulation of the Harper model on optical lattices was envisioned in [33]. In the following discussions, we denote by n_q the total number of qubits including ancilla and workspace qubits, and $N=2^{n_q}$ is the total dimension of the Hilbert space of the quantum computer. We denote n_r with $n_r \leqslant n_q$, the number of qubits describing the Hilbert space of the kicked Harper model [i.e., the wave function evolved through Eq. (4) is N_H dimensional with $N_H=2^{n_r}$], and n_g is the number of elementary quantum gates used for one iteration of the quantum map (4).

A. Exact algorithm

This approach is similar to the one taken in [10] for the quantum simulation of the kicked rotator. In each representation, the value of the cosines is built on a separate register and then transferred to the phase of the wave function by appropriate gates.

If one starts with a N_H-dimensional wave function $|\psi\rangle = \Sigma_{i=0}^{N_H-1} a_i|\theta_i\rangle$ in the θ representation, with $N_H=2^{n_r}$, then the first step is to perform

$$\sum_{i=0}^{N_H-1} a_i|\theta_i\rangle|0\rangle \rightarrow \sum_{i=0}^{N_H-1} a_i|\theta_i\rangle|\cos\,\theta_i\rangle.$$

To this aim, the $2n_r$ values $\cos(2\pi/2^j)$ and $\sin(2\pi/2^j)$, for $j=1,\ldots,n_r$, are first precomputed classically with precision 2^{-n_p} with, for example, $n_p=2n_r$ using a recursive method based on Moivre's formula; then, since $\theta_i=\Sigma_{j=1}^{n_r}\beta_{ij}2\pi/2^j$ with $\beta_{ij}=0$ or 1, one has

$$\exp(i\theta_i) = \prod_{j=1}^{n_r} \exp(i\beta_{ij}2\pi/2^j)$$

$$= \prod_{j=1}^{n_r} [\cos(\beta_{ij}2\pi/2^j) + i\,\sin(\beta_{ij}2\pi/2^j)].$$

This enables to compute $|\cos\,\theta_i\rangle$ for each θ_i in n_r multiplications by $\exp(i2\pi/2^j)$ conditioned by the values of β_{ij}, needing in total $O(n_r^3)$ quantum gates.

Then once the binary decomposition of $\cos\,\theta_i$ is present on the second register, conditional application of the n_r one-qubit gates

$$\begin{pmatrix} 1 & 0 \\ 0 & \exp(-iK2^{-j}/\hbar) \end{pmatrix}$$

yields the state

$$\sum_{i=0}^{N_H-1} a_i \exp[-iK\cos(\theta_i)/\hbar]|\theta_i\rangle|\cos\,\theta_i\rangle.$$

Then the cosines in the last register are erased by running backward the sequence of gates that constructed them, and one ends up with the state

$$\sum_{i=0}^{N_H-1} a_i \exp[-iK\cos(\theta_i)/\hbar]|\theta_i\rangle|0\rangle,$$

which is the result of the action of the unitary operator $\exp[-iK\cos(\hat{\theta})/\hbar]$ on $|\psi\rangle$.

Then the use of the QFT which needs $O(n_r^2)$ quantum gates shifts the wave function to the momentum representation, and exactly the same technique as above enables us to implement the operator $\exp[-iL\cos(\hbar\hat{n})/\hbar]$ in $O(n_r^3)$ quantum gates. A second QFT enables us to go back to the θ representation.

The whole process implements one iteration of the evolution operator $\hat{U}$ in $O(n_r^3)$ operations, with exponential precision. This algorithm is therefore efficient, and precision can be increased exponentially at a cost of polynomial number of operations. On the other hand, the drawback of this approach is the need of several extra registers (one holding the values of the cosines, plus others for the workspace of the computation) and a relatively large number of gates. In the present status of experimental implementations of quantum computers, both the number of qubits and the number of gates that can be applied are very expensive resources. In the following, we will therefore expose two alternative strategies to implement $\hat{U}$, which are much more economical in the use of resources, but involve additional approximations.

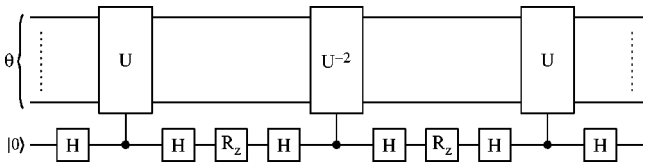

FIG. 4. Gate sequence for slices algorithm. R_z are Z rotations of angle $-\alpha$.

B. Slice method

This technique enables to compute the operator $\hat{U}$ of Eq. (4) without explicitly calculating the cosines. It approximates $\hat{U}$ by a sequence of many operators, each of them being easier to compute. It can be viewed as "slicing" the operator into elementary operators.

As above, we start with a N_H-dimensional wave function $|\psi\rangle=\Sigma_{i=0}^{N_H-1}a_i|\theta_i\rangle$ in the θ representation, with $N_H=2^{n_r}$. In general, suppose we want to perform the operator

$$U_k = e^{-ik\cos(p\hat{\theta})}.$$

In the θ representation, this operator is diagonal, so we just have to multiply each state by the phase $e^{-ik\cos(p\theta)}$. First, we write θ as

$$\theta = \frac{2\pi}{N_H}\sum_{i=0}^{n_r-1} d_i 2^i, \tag{5}$$

where the d_i's are the binary expansion of θ and $N_H=2^{n_r}$. If $p=2^a m$ with m odd, then

$$p\theta = \frac{2\pi m}{N_H}\left(\sum_{i=0}^{n_r-a-1} d_i 2^{i+a}\right) \mathrm{mod}\ 2\pi.$$

Thus U_k is equivalent to applying

$$e^{-ik\cos(m\theta)}$$

on the n_r-a first qubits. In the following, we will suppose that p is odd ($a=0$) for the sake of simplicity.

With the help of one ancilla qubit, let us perform the following sequence, where all gates are applied to the ancilla (initially set to $|0\rangle$), except for C_U which is the operator U applied on the principal register, controlled by the ancilla (the gate sequence is also displayed in Fig. 4):

$$M(\alpha,U) = HC_U He^{i(\alpha/2)\sigma_z} HC_{U^{-2}} He^{i(\alpha/2)\sigma_z} HC_U H.$$

This product is equal to

$$M(\alpha,U) = \cos^2\frac{\alpha}{2} - \sin^2\frac{\alpha}{2}\frac{U^2+U^{-2}}{2} + i\sin\alpha\frac{U+U^{-1}}{2}\sigma_z - i\sin^2\frac{\alpha}{2}\frac{U^2-U^{-2}}{2i}\sigma_x = 1 + i\alpha\frac{U+U^{-1}}{2}\sigma_z + O(\alpha^2) \quad \text{for } \alpha \ll 1.$$

If we take $U=e^{ip\theta}$,

$$M(\alpha,U) = 1 + i\alpha\cos(p\theta)\sigma_z + O(\alpha^2),$$

since the ancilla qubit is in the $|0\rangle$ state,

$$M(\alpha,U) \approx e^{i\alpha\cos(p\hat{\theta})}.$$

The kick operator can then be performed by $n_s \gg 1$ applications of $M(\alpha,U)$:

$$U_k \approx M(\alpha,U)^{n_s} \text{ with } \alpha = \frac{-k}{n_s}.$$

A more accurate expansion can be obtained by symmetrizing $M(\alpha,U)$:

$$\widetilde{M}(\alpha,U) = M\left(\frac{\alpha}{2},U\right)M\left(\frac{\alpha}{2},U^{-1}\right) = 1 + i\alpha\frac{U+U^{-1}}{2}\sigma_z - \frac{\alpha^2}{2}\left(\frac{U+U^{-1}}{2}\right)^2 + O(\alpha^3).$$

Thus $U_k \approx \widetilde{M}(\alpha,U)^{n_s}$ up to order 2 in α.

In this way, once a certain precision has been fixed, n_s can be chosen such that the error is small enough.

If we apply this strategy to the kicked Harper model, the method is therefore to first compute $\exp[-iK\cos(\hat{\theta})/\hbar]$ through the technique above ($k=K/\hbar, p=1$), then use a QFT to shift to the momentum representation. In the n representation, the operator $\exp[-iL\cos(\hbar\hat{n})/\hbar]$ can be cast in the form above for $\hbar = 2\pi m/N_H$, with $p\to m$, $k\to L/\hbar$, and $\theta \to 2\pi n/N_H$. The use of a QFT then shifts back the wave function to the θ representation.

The evolution of a N_H-dimensional wave function with $N_H=2^{n_r}$ through one time slice is efficient, costing $O(\log N_H)$ quantum operations. Indeed, for n_s slices, one diagonal operator in Eq. (4) is implemented in $4+2(n_r-a)+(n_s-1)[7+2(n_r-a)]$ elementary gates, with $a \leqslant n_r$. The number of slices fixes the precision. If one requires a fixed precision, independent of the number of qubits, then the whole method is efficient, iterating $\hat{U}$ in $O((\log N_H)^2)$ operations (the most costly operation asymptotically being the QFT). However, if one requires the precision to increase with N_H, then the method becomes less efficient. This algorithm is quite economical in qubits, since to simulate a wave function on a Hilbert space of dimension 2^{n_r}, only $n_q=n_r+1$ qubits are needed. One should note that for large number of slices, their computation dominate the computation time although asymptotically the QFT dominates. In all numerical simulations we performed, the slice contribution was indeed dominant.

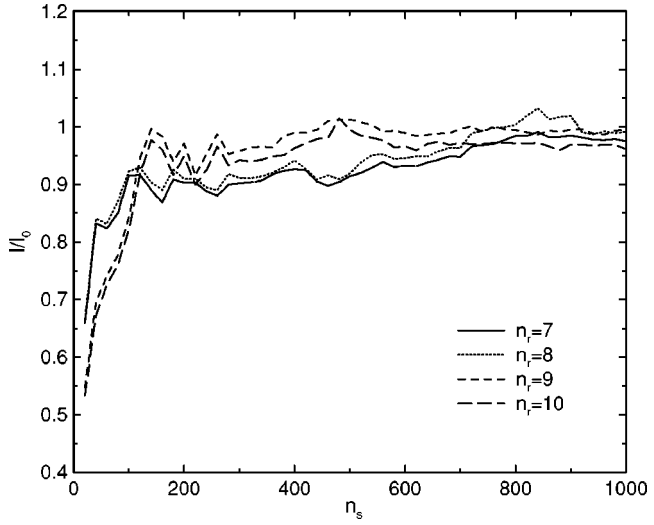

FIG. 5. Localization length computed with the slice method over exact localization length l_0 as a function of number of slices per iteration. Localization length is extracted after $t=1000$ iterations. Initial state is $|\psi_0\rangle=|0\rangle$, with $K=1$, $L=5$, $\hbar/2\pi=(13-\sqrt{5})/82$ (actual value is the nearest fraction with denominator 2^{n_r} with $n_r=n_q-1$).

To precise the accuracy of the method, we show examples of the localization length in the localized regime as a function of number of gates in Fig. 5. The convergence with increasing number of slices (gates) is clearly seen, although for a small number of gates oscillations are present. Data from $n_r=7,8$ and $n_r=9,10$ are close to each other due to the structure of the algorithm: indeed, $\hbar/(2\pi)$ is approximated by its closer approximants m/N_H, and incrementing n_r by 1 changes every other time the value of $\hbar$. No major modification is seen in the numerical data for increasing n_r, indicating that in this regime n_s does not need to be drastically changed with n_r.

One may think that the spectrum is a much more sensitive quantity than the localization length. In Fig. 6, we display the convergence for the spectrum of $\hat{U}$ for K and L small, in a parameter regime close to the fractal "butterfly" visible for the unkicked Harper model (see Fig. 24). The quantities displayed correspond to eigenphases E_a where $\hat{U}|\psi_a\rangle = \exp(iE_a)|\psi_a\rangle$ for some $|\psi_a\rangle$. The matrix of the operator $\hat{U}$ of Eq. (4) is built by evolving through the slice method explained above the basis vectors and then diagonalized. Convergence can be achieved with a few hundred time slices. Due to numerical limitations, we cannot present data for different values of n_r, but we do not expect any drastic modification.

In the subsequent sections, numerical simulations of this algorithm in presence of errors will be performed. To keep the computation time reasonable, we chose to use the slice method with 2×40 slices per iteration for transport properties (Sec. IV). Although the localization length is not exactly the correct one, the system is still localized and enables to study the variation of transport properties in presence of errors and imperfections. For computation of the spectrum (Sec. V), we used 2×100 slices per iteration.

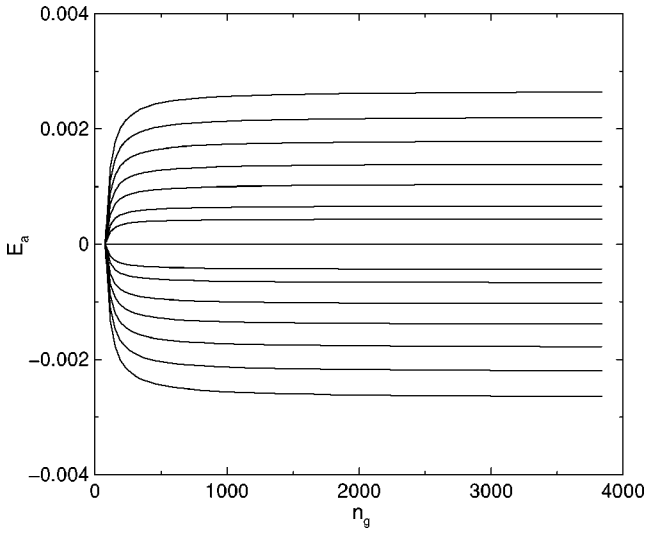

FIG. 6. Eigenphases of Eq. (4) as a function of number of gates with the slice method: only 16 values are shown. Here $n_r=6$ ($n_q=n_r+1$), $\hbar=2\pi/2^6$, $K=L=10^{-3}$.

C. Chebyshev polynomials

In this approach, one uses the QFT as in the preceding methods to shift back and forth between θ and n representations. In each representation, the relevant operator is implemented by using a polynomial approximation of the cosines. Since polynomials can be implemented directly through controlled operations, this avoids the use of additional registers. A commonly used polynomial approximation rests on Chebyshev polynomials.

Chebyshev polynomials (see, for example, [34]) are defined by the recurrence relation

$$T_0(x)=1,$$

$$T_1(x)=x,$$

$$T_n(x)=2xT_{n-1}(x)-T_{n-2}(x) \quad \text{for } n\geqslant 2.$$

They are bounded by -1 and 1 on $[-1,1]$, with their extrema smoothly distributed over this interval. If $f(x)$ is an arbitrary function on $[-1,1]$ and we define, for $j=0,\ldots,M-1$,

$$c_j=\frac{2}{M}\sum_{k=0}^{M-1} f\left[\cos\left(\frac{\pi\left(k+\frac{1}{2}\right)}{M}\right)\right]\cos\left(\frac{\pi j\left(k+\frac{1}{2}\right)}{M}\right),$$

then, for large M,

$$\sum_{j=0}^{M-1} c_jT_j(x)-\frac{1}{2}c_0$$

is a very good approximation of $f(x)$ on $[-1,1]$.

If we truncate this formula to order m,

$$\sum_{j=0}^{m} c_jT_j(x)-\frac{1}{2}c_0,$$

then the error is bounded by $\Sigma_{j=m+1}^{M-1}|c_k|$ and smoothly spread over $[-1,1]$. Practically, the c_k's are always rapidly decreasing, so the error term is dominated by $|c_{m+1}|$ and we can choose a small m while still keeping a good polynomial approximation of $f(x)$.

Let $P(x)$ be a Chebyshev polynomial approximation of $\cos[\pi(x+1)]$. If one wants to perform the operator $U_k=e^{-ik\cos(p\hat{\theta})}$ on a N_H-dimensional vector with $N_H=2^{n_r}$ as in the preceding subsection, then, for $p=1$,

$$U_k\approx e^{-ikP(\hat{\theta}/\pi-1)}.$$

U_k can be decomposed as a product of operators of the form $A_r(\beta)=e^{i\beta\hat{\theta}^r}$.

From Eq. (5),

$$e^{i\beta\theta^r}=\prod_{j_1\cdots j_r} e^{i\beta(2\pi/N_H)^r d_{j_1}\cdots d_{j_r}2^{j_1+\cdots+j_r}}.$$

Since the d_j's are binary digits, $d_{j_1}\cdots d_{j_r}$ is equal to 0 unless all terms are equal to 1. If we denote by $C_{j_1\cdots j_r}(\phi)$ the multicontrolled phase gate, which apply the phase $\exp(i\phi)$ conditionally on the control qubits $j_1\cdots j_r$ (if an index is redundant, then it is counted only once),

$$A_r(\beta)=\prod_{j_1\cdots j_r} C_{j_1\cdots j_r}\left(\beta\left(\frac{2\pi}{N_H}\right)^r 2^{j_1+\cdots+j_r}\right).$$

Since all these gates commute and since all the gates used for the construction of A_r are also present in the development of $A_{r'}$ for $r'\geqslant r$, then all the terms of the polynomial P can be applied at the same time as the term of highest order by merging similar gates.

If $p\neq 1$, then p is split into $p=2^a m$ with m odd, as in Sec. III B. The even part 2^a is dealt with by applying U_k only on the n_r-a first qubits. We then multiply the register by m before applying the cosine kick. Since m is coprime with the dimension of the Hilbert space $N_H=2^{n_r}$, this operation is unitary and can be performed without any additional qubit (for example with the circuit in Fig. 7).

If we choose a Chebyshev polynomial approximation of degree d, then the complexity of the algorithm is $O({n_r}^d)$. This method is economical in qubits, and the precision of the approximation is easy to control. On the other hand, the complexity increases with the precision, and this can become prohibitive for very precise simulations. It is nevertheless quite efficient for fixed precision computations, as can be inferred from the fact that it is actually the method used in classical computers to evaluate functions.

In our numerical simulations, we found that a Chebyshev polynomial of degree 6 was enough to get a very good approximation of the wave function. This demands a much larger number of gates than the slice method and scales badly with n_q, in n_q^6 (here $n_q=n_r$ since there are no ancilla or workspace qubit). However, some of the control-phase gates have very small phases and are physically irrelevant. We can then choose a precision threshold and simply drop all the gates

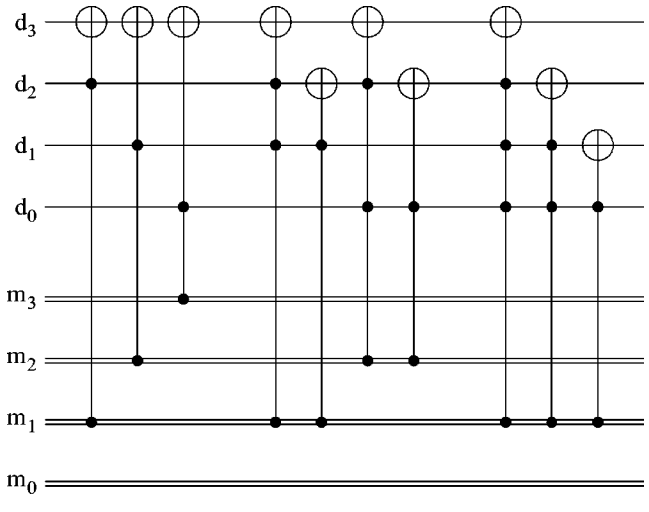

FIG. 7. Circuit for multiplying the quantum register θ (simple lines) by an odd classical number m (double lines).

with phases below this threshold. The distribution of the phases of the gates computing the Chebyshev approximant of degree 6 is displayed in the inset of Fig. 8.

This method of approximation is investigated in Figs. 8 and 9. The localization length as a function of number of gates is displayed in Fig. 8, for the same system parameters as in Fig. 5. In Fig. 9, we display the convergence for the spectrum, in the same regime as in Fig. 6.

In both cases, the convergence is good for maximal number of gates, showing that the polynomial of degree 6 is indeed a good enough approximation in this regime of parameters. A good accuracy is achieved for a lower number of gates, implying that dropping the gates with the smallest

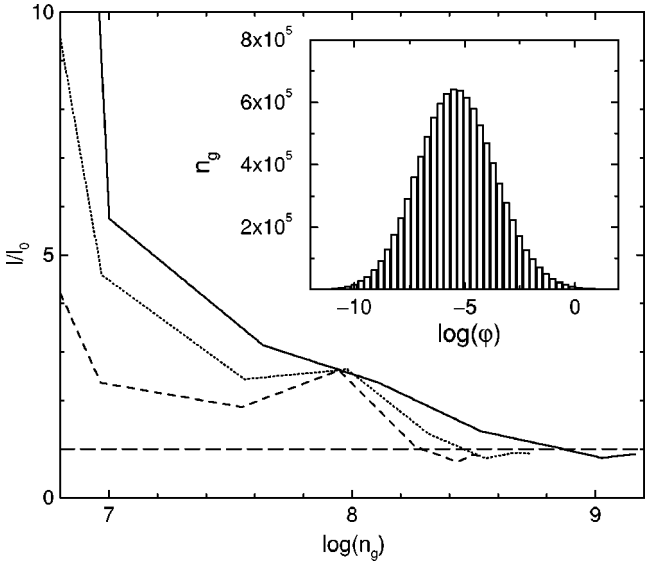

FIG. 8. Localization length computed with the Chebyshev method over exact localization length l_0 as a function of number of gates. System parameters are the same as in Fig. 5, with $n_r=7$ (dashed line), $n_r=8$ (dotted line), and $n_r=9$ (solid line) ($n_q=n_r$). Dashed horizontal line is $l=l_0$. Chebyshev polynomial of degree 6 is taken, keeping gates with the largest phases. Inset: number of gates as a function of their phase. Logarithms are decimal.

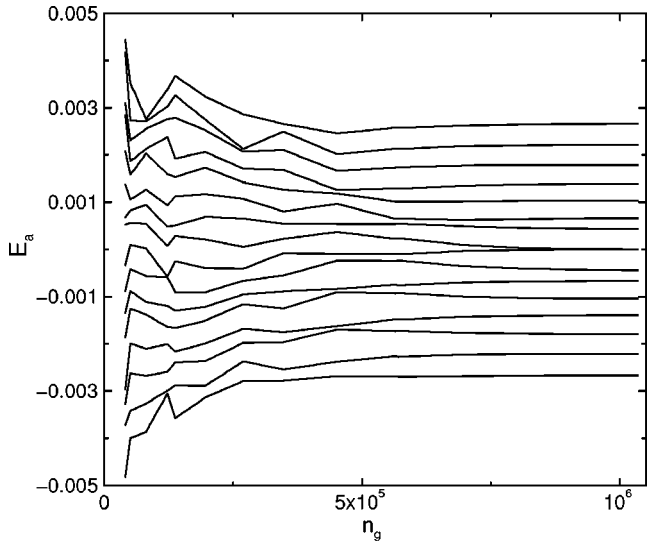

FIG. 9. Eigenphases of Eq. (4) as a function of number of gates with the Chebyshev method. System is the same as in Fig. 6. Chebyshev polynomial of degree 6 is taken, keeping gates with the largest phases. An overall phase factor (global motion of eigenvalues) has been eliminated.

phases can be an effective way to shorten the computation keeping a reasonable accuracy. Still, the data presented lead to the conclusion that even with the elimination of a large number of gates the method is clearly costlier in running time than the slice method to achieve similar precision.

IV. TRANSPORT PROPERTIES: MEASUREMENT AND IMPERFECTION EFFECTS

The three methods exposed above enable to simulate efficiently the effects of the evolution operator $\hat{U}$ of the kicked Harper model on a wave function. This produces the wave function at a given time. An important question concerns which quantities can be obtained through quantum measurement of the registers and if the whole process including measurement is more efficient than classical computation. A separate question but also related to practical efficiency of these algorithms is their stability with respect to errors and imperfections while running them on a realistic quantum computer.

In this section, we will focus on the transport properties of the wave function. We recall that for the kicked Harper model, for small K,L diffusion can only takes place on the small chaotic layer of the stochastic web. Then for larger K,L there is a regime of parameters where all eigenstates are localized and another regime where localized and delocalized eigenstates coexist (see Fig. 3). In these different parameter regimes, we will show that quantities measuring localization properties and diffusion can be obtained on a quantum computer more efficiently than on a classical device, although the gain is usually polynomial. We will then test the resilience to errors of these quantities obtained through the quantum algorithms, in particular through large-scale numerical computations. The error model we chose

corresponds to static internal imperfections. Indeed, physical realization of a quantum computer will never be perfect, and some amount of disorder will always be present. In particular, interactions between qubits, which are needed to build the two-qubit gates, cannot in general be totally eliminated when they are not needed. These static imperfections are not linked to interaction with the outside world; they have been shown to give important effects, which can be larger than the effects of noisy gates [12,35,36]. To model such errors, between each gate we require that the system evolves through the Hamiltonian

$$H_1 = \sum_i (\Delta_0 + \delta_i)\sigma_i^z + \sum_i J_i \sigma_i^x \sigma_{i+1}^x, \tag{6}$$

where the σ_i are the Pauli matrices for the qubit i and the second sum runs over nearest-neighbor qubit pairs on a circular chain. The energy spacing between the two states of a qubit is represented by its average value Δ_0 plus a detuning δ_i randomly and uniformly distributed in the interval $[-\delta/2, \delta/2]$. The detuning parameter δ gives the width of the distribution near the average value Δ_0 and may vary from 0 to Δ_0. The couplings J_i represent the residual static interaction between qubits and are chosen randomly and uniformly distributed in the interval $[-J/2, J/2]$. We make the approximation that this Hamiltonian (6) acts during a time τ_g between each gate which is taken as instantaneous. Throughout the paper, we take in general one single rescaled parameter ε which describes the amplitude of these static errors, with $\varepsilon = \delta\tau_g = J\tau_g$. To probe the transport properties of the kicked Harper model on a quantum computer, we chose to set $\hbar$ constant; in this way, changing the number of qubits is equivalent to changing the size of phase space (adding one qubit doubles the size of the phase space). The only exception is in the first following subsection (near-integrable regime), where the phase-space volume is constant and $\hbar$ varies with the number of qubits. Throughout this section, effects of imperfections will be assessed using the slice method to implement Eq. (4). Therefore the presence of one ancilla qubit implies that $n_q = n_r + 1$ in all of this section.

A. Near-integrable regime: Stochastic web

For K, L very small, the classical system is near integrable: quantum transport is dominated by the presence of invariant curves. Motion from cell to cell can take place only by tunneling effect or by moving in the small chaotic zone around separatrices. In the case $K = L$, this small layer forms a "stochastic web" (see Fig. 2) which extends in both θ and n directions. A wave packet started in this region will slowly diffuse along this web. This process is best seen using quantum phase-space distributions, which allow direct comparisons between classical distributions such as the ones in Fig. 1 and 2 and quantum wave functions.

The Wigner function [37,38] is an example of such quantum phase space distribution. However, it can take negative values, and only a smoothing over cells of area $\hbar$ gives nonnegative values. The use of a Gaussian smoothing leads to the Husimi distribution (see, e.g., [39]) which in our case is defined by the formula

$$h(\theta, n) = \sqrt{\frac{2P}{QN_H^3}} \times \left| \sum_{m=n-N_H/2+1}^{n+N_H/2} \psi(m) e^{-(\pi P/N_H Q)(m-n)^2} e^{2i\pi m\Theta/N_H} \right|^2, \tag{7}$$

where the Gaussian for simplicity is truncated for values larger than $N_H/2$, $\psi(m)$ is the wave function in momentum representation, P (Q) is the number of cells in the momentum (position) direction, $N_H = 2^{n_r}$ is the dimension of the Hilbert space, and $\Theta = N_H\theta/(2\pi Q)$. We note that methods to compute phase-space distributions on a quantum computer were discussed in [13,32,40].

In Fig. 10 we show the spreading of a wave packet along the stochastic web for different numbers of qubits and different strengths of imperfections. In this picture, the size of the classical phase space is fixed, and the number of qubits gives the value of $\hbar$. A diffusion process is observed, which can be related both to the classical diffusion on the stochastic web (Fig. 2) and to the effect of quantum tunneling from cells to cells. The diffusion constant is seen from Fig. 10 to depend on $\hbar$; it also depends on K, L (data not shown) and is clearly different from the classical diffusion constant (compare the different times in Figs. 2 and 10). In this near-integrable regime, the tunneling process is quite complicated and was recently studied in [29]. In the same figure, one can see that with moderate levels of imperfections the exact Husimi distribution is well reproduced by the algorithm.

To probe transport properties in this regime, one can start a wave packet in the stochastic web and let it evolve. After a certain number of time steps, the diffusion constant can be obtained from measurement of the wave function. As the number of components of the wave function or of the Husimi distribution becomes exponentially large as n_r increases, the best way is to use coarse-grained measurements: measuring only the first qubits adds up the amplitudes squared of many neighboring components and limits the number of measurements to a fixed value. This can be done to the wave function directly in the momentum or position representation or to the Husimi function provided all the values are kept on a quantum register. For example, the Husimi-like function developed in [13] can be obtained by modified Fourier transform from the wave function and allows the use of coarse-grained measurements. If one starts a wave packet on the stochastic web, it will diffuse according to the law $\langle s(t)^2 \rangle \approx D_s t$, with s being a distance in phase space and D_s the diffusion constant. Performing time evolution up to a time t^* requires t^* quantum operations multiplied by logarithmic factors. At this stage, a fixed number of coarse-grained measurements is enough to give an approximation of D_s. On a classical computer, one can truncate the Hilbert space up to the maximal dimension effectively used in the calculation, which is of the order $\sqrt{t^*}$. Propagating the wave packet will cost $t^* \sqrt{t^*}$ classical operations, after which D_s can be obtained. Therefore the quantum computation is polynomially faster than the classical one. Methods which use an ancilla qubit to measure the value of phase-space distributions at a given point such

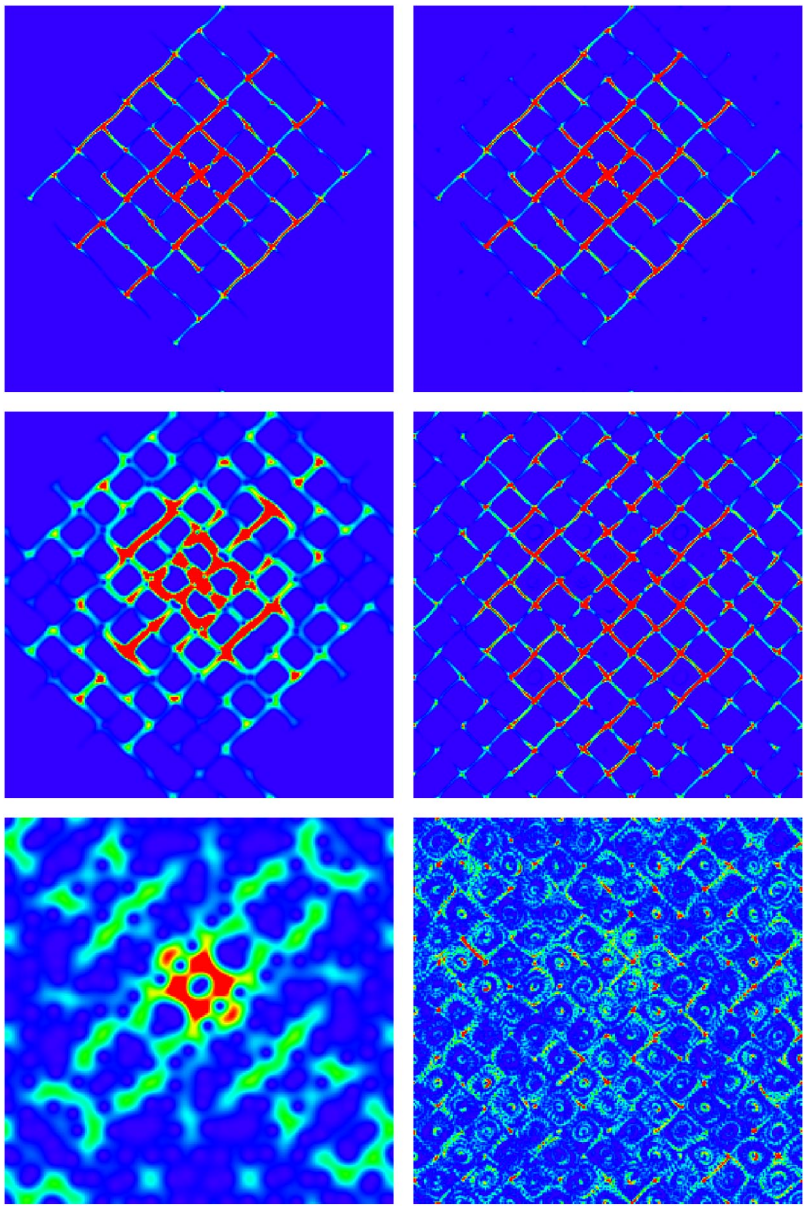

FIG. 10. (Color online) Example of Husimi distribution of a wave packet spreading on the stochastic web; here $K=L=0.5$, $\hbar=2\pi\times 64/2^{n_r}$ (8×8 cells), initial state is a Gaussian wave packet of area $\hbar$ started half a cell above the center of the figure, after 100 iterations using 2×40 slices per iteration. Left: $\varepsilon=0$ and from top to bottom $n_r=14$, $n_r=11$, $n_r=8$ ($n_q=n_r+1$). Right: $n_r=14$ and from top to bottom $\varepsilon=10^{-6}$, $\varepsilon=10^{-5}$, $\varepsilon=10^{-4}$. Color/grayness is related to amplitude of the Husimi function, from zero (blue/black) to maximal value (red/white). Compare with the classical diffusion in Fig. 2.

as the ones in [32,40] will necessitate extra measurements since they cannot be used to perform coarse-grained measurements efficiently. Still, by reducing K,L as n_r is increased, one can keep the number of large components of the Husimi function of the wave packet of order N_H (instead of N_H^2). In this case, the Husimi function measured on the ancilla qubit of [32] is efficiently measurable. This is formally an exponential gain over direct classical simulation since measuring one component of the Husimi distribution at a fixed time t will be logarithmic in N_H. The same happens for coarse-grained measurements at fixed t. Still, as $\hbar$ goes to exponentially small values the dynamics for fixed t will become very close to the classical one, so it is unclear which new information can be gained this way.

To clarify the stability of these algorithms with respect to errors, in Fig. 11 we show quantitatively the effects of imperfections on the Husimi distributions for a wave packet spreading on the stochastic web for various numbers of qubits and imperfection strengths. We computed the time scale t_h for various parameter values, t_h being the time (number of iterations) for which the error on the Husimi functions is half the mean value of that function on the stochastic web.

The numerical data suggest the law

$$t_h \approx C_h/(\varepsilon^{\alpha} n_q^{\beta}), \tag{8}$$

with $\alpha=1.02\pm 0.02$ (compatible with $\alpha=1$) and $\beta=1.23\pm 0.09$ with $C_h\approx 0.007$. This law is polynomial in both ε and n_q, which indicates that even though individual values of the Husimi function can be exponentially small, the effect of imperfections remains small compared to these individual values for a polynomial time. This means that such quantities can be reliably obtained in presence of moderate levels of imperfections. More work is needed to understand the precise origin of the law (8). We note that in [11] where random noise in the quantum gates were used as main source of errors a similar polynomial (but different) law was found for the relative error on the Husimi function.

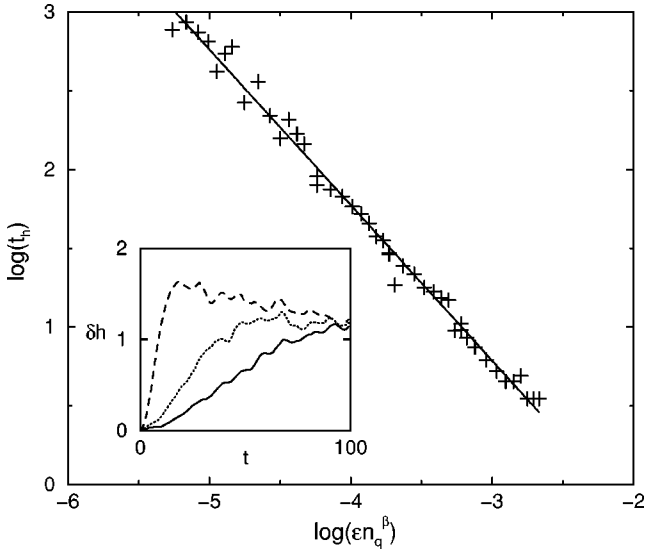

FIG. 11. Effects of imperfections on the Husimi distribution of a wave packet spreading on the stochastic web; here $K=L=0.5$, $\hbar=2\pi\times 64/2^{n_r}$ (8×8 cells), initial state is a Gaussian wave packet of area $\hbar$ started half a cell above the center of the Fig. 2, and iterations are made by the slice method using 2×40 slices per iteration. Straight line is the law (8) with $\alpha=1$ and $\beta=1.23$. Crosses corresponds to various values of ε ($10^{-6}\leqslant\varepsilon\leqslant 10^{-4}$) and n_r ($5\leqslant n_r\leqslant 14$, with $n_q=n_r+1$); averages were made over all Husimi components inside the stochastic web and up to 100 realizations of disorder for each ε value. Inset: average relative error of the Husimi function $\delta h=\langle|h_\varepsilon-h_0|\rangle/\langle h_0\rangle$ on the stochastic web for $\varepsilon=10^{-4}$ (dashed line), $\varepsilon=10^{-4.5}$ (dotted line), $\varepsilon=10^{-5}$ (solid line), and $n_r=10$ ($n_q=n_r+1$). Average is taken over all Husimi components inside the stochastic web and 10 realizations of disorder. Logarithms are decimal.

B. Localized regime

When K is large enough for the chaotic zone to take most of the classical phase space, a classical particle will propagate diffusely in phase space. In contrast, for moderate values of the parameter K, all the eigenstates of the evolution operator $\hat{U}$ of (4) are localized (see Fig. 3). This localization is a purely quantum phenomenon due to interference effects and similar to the Anderson localization of electrons in solids. In this parameter regime, an initial wave packet will have projections on only a small number of exponentially localized eigenstates. Thus after a few iterations of the map, the wave packet will stop spreading and stay in a region of momentum space of size given by the localization length. An example of such a wave function is shown in Fig. 12.

In this regime, it is possible to measure the localization length l efficiently. Indeed, most of the probability is concentrated in a domain of size l. If one performs a coarse grained measurement of the wave function—i.e., only the most significant qubits are measured—the number of measurements will set the precision in units of l. Thus once the desired relative precision is fixed, the number of measurements is independent of l or n_q. Nevertheless, if one starts from an easily prepared initial wave packet—for example, on a single momentum state—one has to evolve it long enough to reach

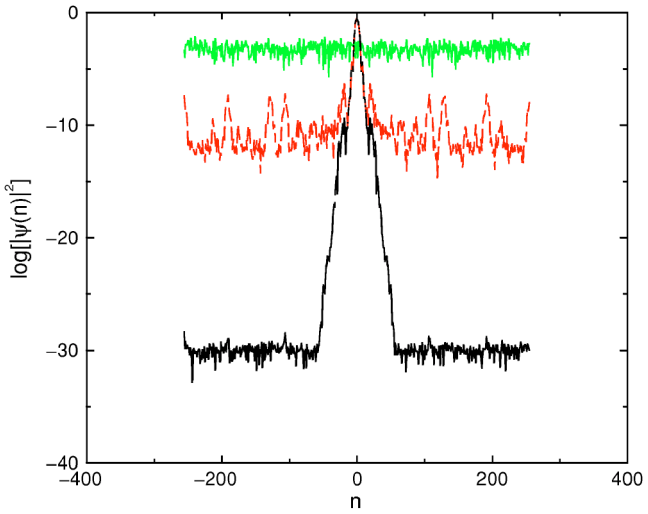

FIG. 12. (Color online) Example of wave function in the localized regime. Here $K=1$, $L=5$, $\hbar/(2\pi)=(13-\sqrt{5})/82$ (actual value is the nearest fraction with denominator 2^{n_r}), initial state is $|\psi_0\rangle=|0\rangle$, after 1000 iterations using 2×40 slices per iteration, $n_r=8$ ($n_q=n_r+1$), from bottom to top $\varepsilon=0$ (black, solid line), $\varepsilon=10^{-7}$ (red, dashed line), and $\varepsilon=10^{-3}$ (green, solid line). In the center, the first two curves are superposed and indistinguishable. Logarithm is decimal.

a saturation regime where the wave function is spread on a domain of size $\approx l$. Classically, in the parameter regime where the system is chaotic, the dynamics is diffusive $\langle n(t)^2\rangle\approx Dt$ with a diffusion constant D which depends on parameters. One can expect the wave packet to follow for short time this diffusive behavior which will stop when a spreading comparable to the localization length is reached. In this case, the wave packet needs to be evolved until a time $t^*\approx l^2/D$. Classically, one needs to evolve a vector of dimension $\sim l$ until the time t^*; this needs $\sim l^3$ classical operations. On a quantum computer, once the precision is set, the three algorithms above need only a logarithmic number of gates to perform one iteration, so the total number of gates is $\sim l^2$. This gives a polynomial improvement for the quantum algorithm. It is known that in the delocalized phase, the wave packet can spread ballistically for some regimes of parameter. If this extends to short times and to the localized regime, then the gain becomes quadratic.

In Fig. 12, an example of a localized wave function is shown for different imperfection strengths. At $\varepsilon=0$, the exponential localization is clearly visible, the exponential decay being leveled off at very small values ($\approx 10^{-30}$) only by numerical roundoff. For larger values of ε, the localized peak is still visible with the correct amplitude, but a larger and larger background is visible, until the peak disappears.

To analyze in a more precise way the effects of imperfections, we have to specify the observable that is used to get the localization length. On a classical computer, different data analyses can be used to calculate the localization length from knowledge of the wave function. A first way consists in extracting the second moment of the wave function $\langle(\Delta n)^2\rangle$, which gives an estimate of l once the saturation regime is reached. One can also compute the inverse participation ratio

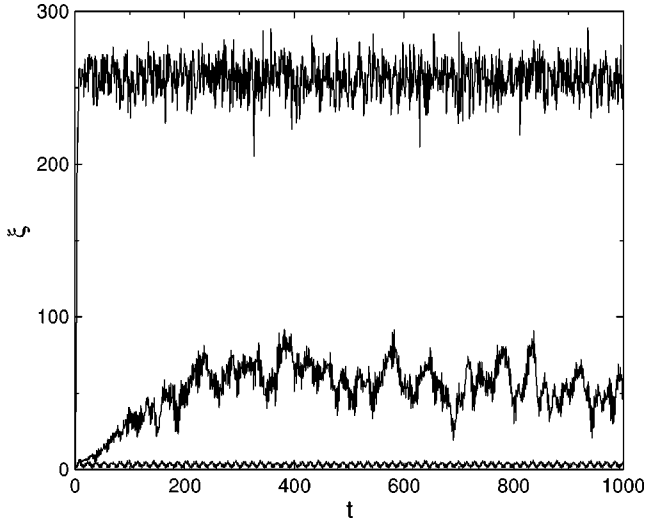

FIG. 13. Example of IPR with imperfections as a function of time, in the localized regime. Parameters values are the same as in Fig. 12, $n_r=8$ ($n_q=n_r+1$), from bottom to top $\varepsilon=0$, $\varepsilon=10^{-7}$, $\varepsilon=10^{-4}$, and $\varepsilon=10^{-3}$. Data from $\varepsilon=0$ and $\varepsilon=10^{-7}$ are indistinguishable.

(IPR) $\xi=1/\Sigma_n|\psi(n)|^4$. For a wave function uniformly spread over M states this quantity is equal to M, and therefore it also gives an estimate of the localization length. At last, l can be measured directly by fitting an exponential function around maximal values of ψ.

For an exact wave function, all three quantities give similar results. On a quantum computer, they may have very different behavior with respect to imperfection strength. Indeed, it was shown in general [11,41] that the second moment is exponentially sensitive to the number of qubits in presence of imperfections, making it a poor way to get information about transport properties. The IPR was shown [41] to be polynomially sensitive to both number of qubits and imperfection strength. Still, the IPR may be difficult to measure directly on a quantum computer. On the other hand, the direct measurement of l by fitting an exponential curve on a coarse-grained measure of the wave function was shown in [41] to be an effective way to extract l from a quantum computation of the wave function. It is therefore interesting to study the behavior of both latter quantities with respect to imperfections.

In Fig. 13, the time evolution of the IPR is shown for different values of the imperfection strength. For $\varepsilon=0$, the wave packet first spreads for $t<t^*$, and then the IPR becomes approximately constant and close to the localization length. For larger values of ε, the wave packet spreads to much larger parts of phase space, but the IPR still saturates after some time to a value which depends on ε and n_q.

The average value of this saturation value is shown in Fig. 14 as a function of ε for different values of n_q. Figure 15 shows the localization length obtained from curve fitting for the same wave functions. For large enough values of ε, the IPR grows very quickly, in a manner which seems exponentially dependent on n_q. The result of the curve-fitting strategy is roughly similar, but shows an intermediate regime ($\varepsilon\approx10^{-4}$ for our data) where it is still reasonably close to the

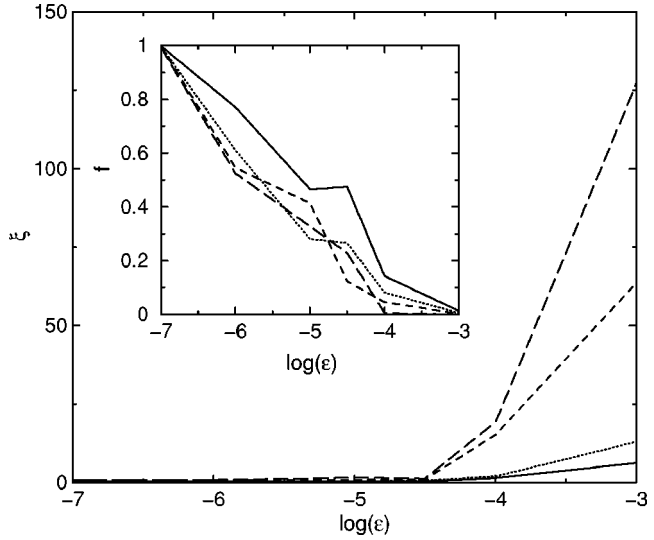

FIG. 14. IPR as a function of imperfection strength in the localized regime. Parameters values are the same as in Fig. 12, with $n_r=7$ (solid line), $n_r=8$ (dotted line), $n_r=9$ (dashed line), and $n_r=10$ (long-dashed line) ($n_q=n_r+1$). Averages were made over up to 10 realizations of disorder. Inset: fidelity as a function of imperfection strength in the localized regime, with same parameter values and line codes as in the main figure. Logarithms are decimal.

exact value while the IPR is already quite far off. This can be understood qualitatively from the data shown in Fig. 12. Indeed, the effect of moderate static imperfections is to create a larger and larger background over which the localization peak is superimposed. The IPR is sensitive to the presence of this background, while by its very definition the curve-fitting strategy isolates the localization peak from the background and is therefore more robust. The data presented in Fig. 15 show that this peak keeps its shape with relatively good accuracy until its final disappearance, even though a large

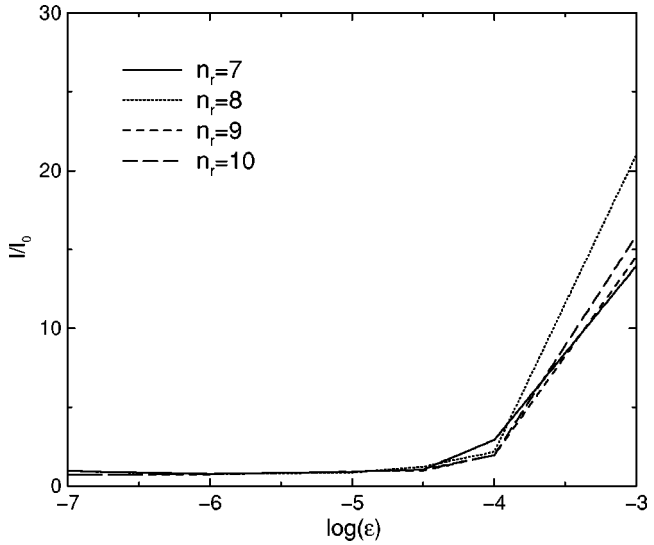

FIG. 15. Localization length as a function of imperfection strength in the localized regime. Parameters values are the same as in Fig. 12, with averages made over up to 10 realizations of disorder. Logarithm is decimal.

chunk of its amplitude has been transfered elsewhere by imperfections. The inset of Fig. 14 shows the fidelity of the same wave functions $[f(t)=|\langle\psi(t)|\psi_\varepsilon(t)\rangle|^2$ where $|\psi(t)\rangle$ is the exact wave function and $|\psi_\varepsilon(t)\rangle$ the one in presence of imperfections]. It is interesting to note that the localization length and IPR can be quite well reproduced even for values of ε where the fidelity is already quite low.

A more precise analysis can be developed from the effect of imperfections on the eigenstates of the unperturbed evolution operator $\hat{U}$ in Eq. (4). These eigenstates $|\psi_a\rangle$ can be written as a sum over momentum states $|m\rangle$, which coincide with quantum register states of the quantum computer when the system is in momentum representation:

$$|\psi_a\rangle = \sum_{m=1}^{N_H} c_a^m |m\rangle. \tag{9}$$

In the localized regime, the eigenstates $|\psi_a\rangle$ are localized with localization length l; therefore, the c_a^m are significant only for $\sim l$ values of m, with an average value of $1/\sqrt{l}$. Using perturbation theory, one can estimate the typical matrix element of the imperfection Hamiltonian (6) between eigenstates. For the first term of Eq. (6), this gives

$$V_{typ} \sim \left| \langle\psi_b| \sum_{i=1}^{n_q} \delta_i \widehat{\sigma_i^z} \tau_g n_g |\psi_a\rangle \right| \sim \tau_g n_g \left| \sum_{m,n=1}^{N_H} c_a^m c_b^{n*} \langle n| \sum_{i=1}^{n_q} \delta_i \widehat{\sigma_i^z} |m\rangle \right|, \tag{10}$$

where $N_H=2^{n_r}$ is the dimension of Hilbert space on which $\hat{U}$ acts, τ_g is the time for one gate, and the term due to Δ_0 in Eq. (6) is not taken into account since it can be eliminated easily. This estimate (10) is an approximation, since the action of Eq. (6) is separated from the action of $\hat{U}$ and in reality they are intertwined and do not commute. In Eq. (10), only $\sim l$ neighboring quantum register states are coupled through n_q terms of different detuning δ_i (with random sign). This term therefore gives on average $\varepsilon n_g \sqrt{n_q}/\sqrt{l}$. The second term of Eq. (6) in the same approximation will be the sum of n_q terms, each coupling one state $|m\rangle$ with another state differing by two neighboring qubits $|n\rangle=|m+r\rangle$. So a state $|\psi_a\rangle$ is coupled significantly only to states $|\psi_b\rangle$ localized at a distance r in momentum from $|\psi_a\rangle$. Therefore the same estimate applies, and overall one can estimate $V_{typ} \sim \varepsilon n_g \sqrt{n_q}/\sqrt{l}$.

One can suppose that the IPR will become large when perturbation theory breaks down. This happens when V_{typ} is comparable to the distance between directly coupled states Δ_c. From the arguments above, one expects that one state is coupled to $\sim l$ states so that this distance is $\Delta_c \sim 1/l$. The threshold when IPR or localization length become large is therefore $V_{typ} \sim \Delta_c$ which corresponds to

$$\varepsilon_c \approx C_1/(n_g \sqrt{n_q} \sqrt{l}), \tag{11}$$

where C_1 is a numerical constant and n_g is number of gates per iteration, n_q number of qubits, and l the localization length. Figure 16 is compatible with this scaling, with $C_1/\sqrt{l} \approx 0.3$. We note that this threshold is similar to the threshold for the transition to quantum chaos presented for a quantum computer not running an algorithm in [35].

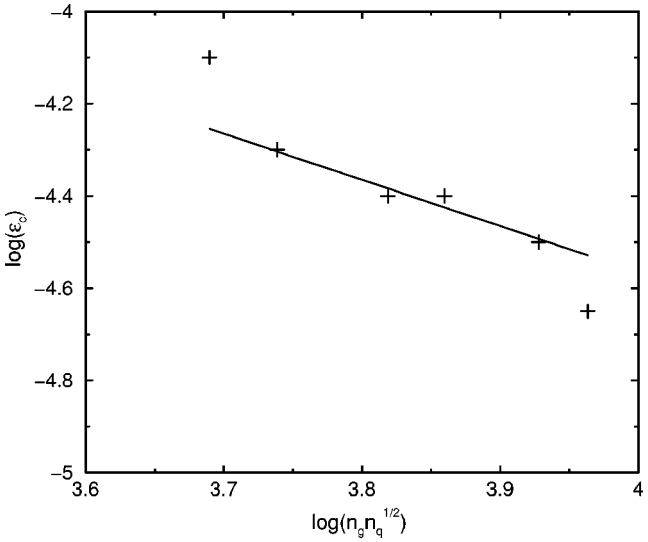

FIG. 16. Critical value of ε (error strength) as a function of parameters for $K=2$, $L=27$, with other parameter values the same as in Fig. 12. ε_c is defined by a saturation value of IPR twice the unperturbed value. Averages were made with up to 10 realizations of disorder. Solid line is the formula (11). Logarithms are decimal.

When perturbation theory breaks down, it is usually expected from earlier works on quantum many-body physics [35,42] that the system enters a Breit-Wigner regime where the local density of states is a Lorentzian of half-width $\Gamma \approx 2\pi|V_{typ}|^2/\Delta_c$ according to the Fermi golden rule. This implies that the IPR grows like $\Gamma/\Delta_n \sim \varepsilon^2 n_g^2 n_q N$, where $\Delta_n \sim 1/N_H \sim 1/N$ is the mean level spacing ($N=2N_H$ since there is an ancilla qubit). This is not confirmed by the data shown on Fig. 17, which suggest that the IPR scales like ε. This indicates that in our system we are in a regime different from the golden rule (Breit-Wigner) regime.

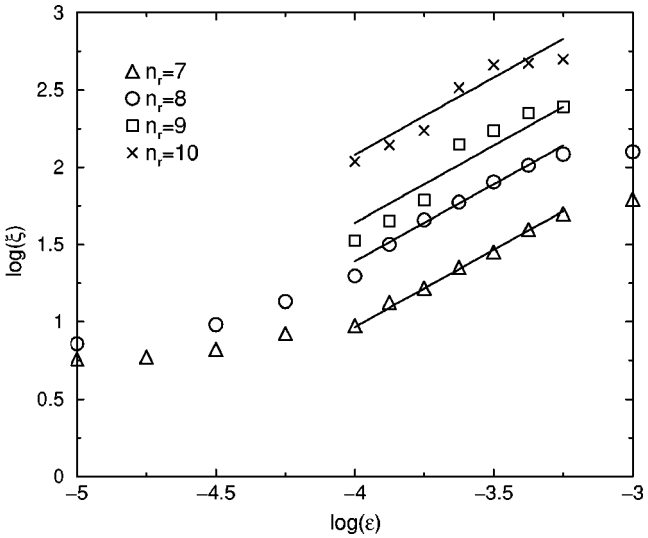

FIG. 17. IPR as a function of ε. Parameters values are the same as in Fig. 16. Solid lines correspond to the dependence $\xi \propto \varepsilon$. Logarithms are decimal.

Such a regime is present for large perturbation strength in many-body systems. It is indeed known that for large enough values of the couplings, the system leaves the golden rule regime and enters a new regime where the local density of states is a Gaussian of width given by the variance σ. The variance can be approximated by $\sigma^2 \sim \Sigma_{b\neq a} V_{typ}^2 \sim \varepsilon^2 n_g^2 n_q$. In this regime the IPR is given by $\sigma/\Delta_n \sim \varepsilon n_g \sqrt{n_q N}$, which is consistent with data from Figs. 14 and 17. This regime is known to supersede the golden rule regime for $\Gamma > \sigma$, which should therefore be the case for our system. This implies that the relevant time scale for the system to remain close to the exact one is $1/\sigma$. For the largest values of n_q, the data in Fig. 17 show some departure from this law, which may be due simply to statistical fluctuations (the averaging is made over more instances for smaller n_q) or a shift toward the golden rule regime for large n_q.

The scaling laws obtained in this regime show that for $\varepsilon < \varepsilon_c$, with ε_c given by Eq. (11), the system is still localized in presence of imperfections, and the localization length is close to the exact one. In this case, the localization length is correct for very long times, much longer than for example the fidelity decay time. For larger ε, the system with imperfections is delocalized. We still expect it to be close to the exact one up to a time $\sim 1/\sigma \sim 1/(\varepsilon n_g \sqrt{n_q})$.

C. Partially delocalized regime

For larger values of K at L fixed, the system enters a partially delocalized region. In this regime, there is a coexistence of localized and delocalized eigenstates. An initial wave packet will have significant projections on all delocalized eigenstates but only on neighboring localized eigenstates. After a certain number of time steps (kicks) the part corresponding to delocalized states will spread in all the system, while the localized part will remain close to the initial position. Figure 18 shows an example of a wave packet initially at $n=0$ after 100 iterations in this regime, displaying an exponential peak corresponding to localization superimposed on a plateau which spreads with time to larger and larger momentum. It is known that the spreading of the wave packet in this regime (for large enough time) is ballistic away from the line $K=L$ and diffusive on this line.

In this regime, as above a coarse-grained measurement can give the localized part with moderate accuracy, thus enabling one to compute the localization length. As in the preceding part, the gain over classical computation will be polynomial. As concerns the delocalized part of the wave function, it seems at first sight that getting information on it is difficult, since it takes very long time to reach its saturation distribution (it has to spread diffusively or ballistically through the whole system), and this distribution itself is spread over the exponentially large system. Still, after a time large enough for the wave packet to spread beyond the localization length, the structure of the wave function can be seen very clearly from coarse-grained measurements whose number is on the order of the localization length. Once such a coarse-grained measurement has been performed and the localization length found by fitting an exponential function around the maximum, the relative importance of the plateau

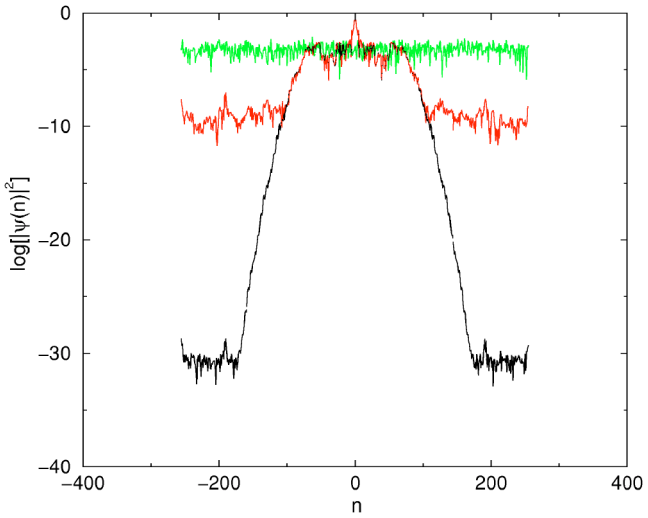

FIG. 18. (Color online) Example of wave function in the partially delocalized regime. Here $K=2$, $L=5$, $\hbar/(2\pi)=(13-\sqrt{5})/82$ (actual value is the nearest fraction with denominator 2^{n_r}), initial state is $|\psi_0\rangle=|0\rangle$, after 100 iterations using 2×40 slices per iteration, $n_r=8$ ($n_q=n_r+1$), from bottom to top $\varepsilon=0$ (black, solid line), $\varepsilon=10^{-7}$ (red, dashed line), and $\varepsilon=10^{-3}$ (green, solid line). In the center, the first two curves are superposed and indistinguishable. Logarithm is decimal.

can be found by subtracting the localized part. Even though the plateau has not yet reached its final distribution, its integrated probability is related to the number of eigenstates which are delocalized at these parameter values. This information enables us to monitor the transition precisely for different values of K and L, nontrivial information as seen from Fig. 3. The number of operations for classical and quantum algorithms are the same as for the localization length, and therefore the same polynomial gain can be expected. Another quantity which can be readily obtained is the quantum diffusion constant. Indeed, away from the line $K=L$, it is known that a quantum wave packet initially localized in momentum will spread anomalously (ballistically) with the law $\langle n^2(t)\rangle \approx D_a t^2$. Classically, estimating the diffusion constant requires one to simulate the system until some time t^*. This requires one to evolve $\sim t^*$ quantum states until the time t^*, making the total number of operation $\sim (t^*)^2$. On a quantum computer, one time step requires a logarithmic number of operations, so the total number of operations is $\sim t^*$ (t^* iterations followed by a constant number of coarse-grained measurements), a quadratic gain compared to the classical algorithm. Close to the line $K=L$, the quantum diffusion becomes normal with the law $\langle n^2(t)\rangle \approx D_n t$. In this regime, the same computation gives a number of operation $\sim (t^*)^{3/2}$ classically compared to $\sim t^*$ for the quantum algorithm, with still a polynomial gain. Such computations can give quite interesting results, in particular to specify precisely which kind of diffusion is present in the vicinity of the line $K=L$, a question which is not definitively settled.

Effects of different strengths of imperfections can be seen in Fig. 18. For moderate values of ε, a flat background of larger and larger amplitude is created by the imperfections. When this background reaches the values of the plateau due

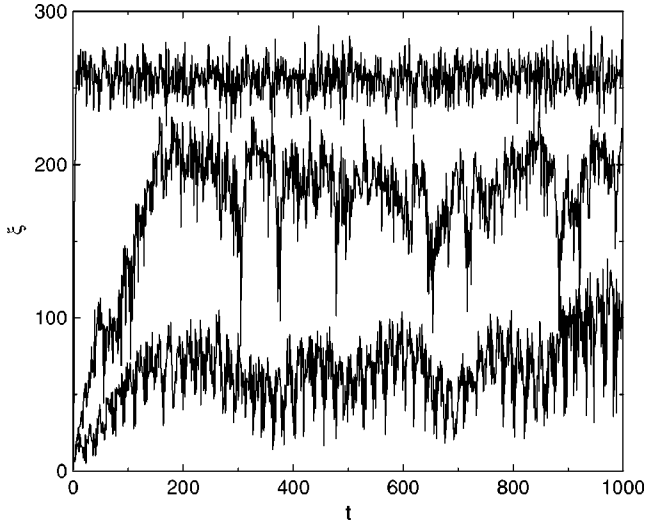

FIG. 19. Example of IPR in presence of imperfections as a function of time in the transition regime. Here $K=4$, $L=5$, $\hbar/(2\pi)=(13-\sqrt{5})/82$ (actual value is the nearest fraction with denominator 2^{n_r}), initial state is $|\psi_0\rangle=|0\rangle$ with 2×40 slices per iteration, $n_r=8$ ($n_q=n_r+1$), from bottom to top $\varepsilon=0$, $\varepsilon=10^{-7}$, $\varepsilon=10^{-4}$, and $\varepsilon=10^{-3}$. Data from $\varepsilon=0$ and $\varepsilon=10^{-7}$ are indistinguishable.

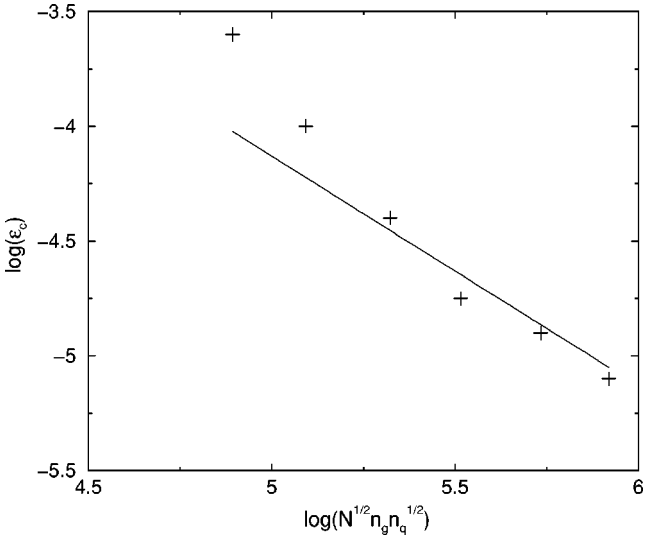

FIG. 20. Critical value of ε (error strength) as a function of parameters for $K=10$, $L=27$ with other parameter values the same as in Fig. 18. ε_c is defined by a saturation value of IPR twice the unperturbed value. Averages were made with up to 10 realizations of disorder. Solid line is the formula (12). Logarithms are decimal.

to delocalized states, information on these delocalized states is lost, but the localized peak remains until ε is large enough to destroy it. This is visible also in Fig. 19 which displays the time evolution of a wave function in this transition region. The data for $\varepsilon=0$ show the spreading of the wave packet due to delocalized eigenstates; the IPR does not reach the dimension of Hilbert space since part of the amplitude does not spread due to localized states. For intermediate values of ε, the spreading concerns more and more of the total amplitude, increasing the IPR, until a large enough value of ε is reached and the wave function is completely delocalized.

In this regime, the analysis of the preceding section should be modified. Indeed, a certain fraction β of the Floquet eigenstates $|\psi_a\rangle$ of $\hat{U}$ (unperturbed) in Eq. (4) are not localized. For these delocalized states, the c_a^m of Eq. (9) have small nonzero values $\sim 1/\sqrt{N_H}$ for all m. The estimation $V_{typ}\sim \varepsilon n_g\sqrt{n_q}/\sqrt{l}$ for the typical matrix element of the imperfection Hamiltonian (6) between eigenstates $|\psi_a\rangle$ and $|\psi_b\rangle$ remains correct only if $|\psi_a\rangle$ and $|\psi_b\rangle$ are both localized.

If $|\psi_a\rangle$ and $|\psi_b\rangle$ are both delocalized, one has $c_a^m\sim c_b^n \sim 1/\sqrt{N_H}$ in Eq. (10) for most m,n. This implies that the quantities $\Sigma_{m=1}^{N_H} c_a^m c_b^m$, previously of order $1/\sqrt{l}$, becomes $\sim 1/\sqrt{N_H}$ (sum of N_H terms of order $\sim 1/N_H$ with random signs). This modifies the estimate for V_{typ}: with the same reasoning as in the localized case, one has $V_{typ}\sim \varepsilon n_g\sqrt{n_q}/\sqrt{N_H}$.

If one of the states $|\psi_a\rangle$ and $|\psi_b\rangle$ is localized and the other one delocalized, then $\Sigma_{m=1}^{N_H} c_a^m c_b^m$ is the sum of l terms of order $\sim 1/(\sqrt{l}\sqrt{N_H})$ with random signs, which is of order $\sim 1/\sqrt{N_H}$. This gives the same estimate $V_{typ}\sim \varepsilon n_g\sqrt{n_q}/\sqrt{N_H}$ for the matrix element as if both states were delocalized.

Therefore, if a proportion β of the unperturbed Floquet eigenstates are delocalized, both localized and delocalized eigenstates will have matrix elements of order $V_{typ}\sim \varepsilon n_g\sqrt{n_q}/\sqrt{N_H}$ with βN_H other eigenstates. This will be the dominant effect, since these couplings lead perturbation theory to break down much earlier than for the purely localized system. Indeed, V_{typ} is comparable to the distance between directly coupled states $\Delta_c\sim 1/N_H\sim 1/N$ (since $N=2N_H$) for $\varepsilon n_g\sqrt{n_q}/\sqrt{N}\sim 1/N$, which corresponds to

$$\varepsilon_c \approx C_2/(n_g\sqrt{n_q}\sqrt{N}), \tag{12}$$

where C_2 is a numerical constant, n_g the number of gates per iteration, n_q the number of qubits, and $N=2^{n_q}$ the dimension of the Hilbert space of the quantum computer. Figure 20 is compatible with this scaling, with $C_2\approx 7.4$.

In this regime, the critical interaction strength drops therefore *exponentially* with the number of qubits, in sharp contrast with the localized regime. This effect has been noted for a different system in [43] and is similar to the enhancement of weak interaction in heavy nuclei [44]. The physical mechanism is that the much smaller coupling term between states is compensated by the even smaller distance in energy between coupled states. This result implies that even for moderate number of qubits, a small interaction strength is enough to modify enormously the long-time behavior of the system: saturation values of the IPR are very much affected by the perturbation, much more so than in the localized regime. However, for short time the behavior of the system should be close to the unperturbed one, implying that the measures suggested to get interesting information, such as relative size of the plateau and diffusion constants can still be accessible.

Figure 21 shows examples of the growth of the IPR as a function of K and imperfection strength. In the partially delocalized zone, the figure shows a growth of the IPR with K, which is strongly affected by imperfections. An interesting quantity is the value of the transition point between localized

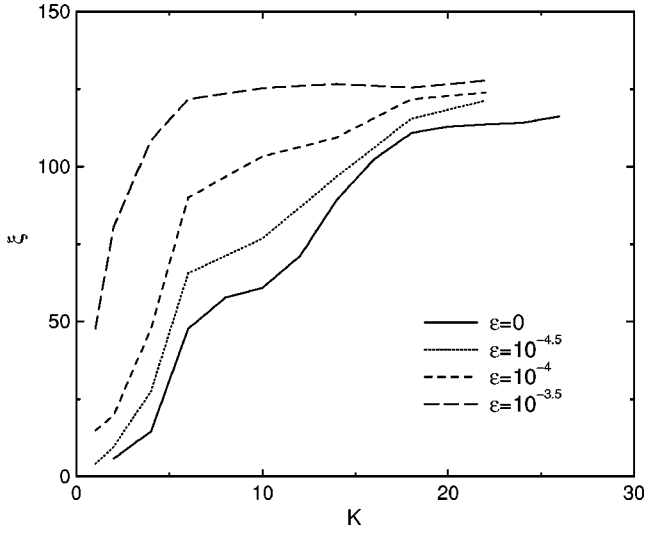

FIG. 21. IPR in presence of imperfections as a function of K in the transition regime. Here $L=27$, $\hbar/(2\pi)=(13-\sqrt{5})/82$ (actual value is the nearest fraction with denominator 2^{n_r}), initial state is $|\psi_0\rangle=|0\rangle$, IPR is shown after 100 iterations using 2×40 slices per iteration, and $n_r=8$ ($n_q=n_r+1$), with averages made over 10 realizations of disorder.

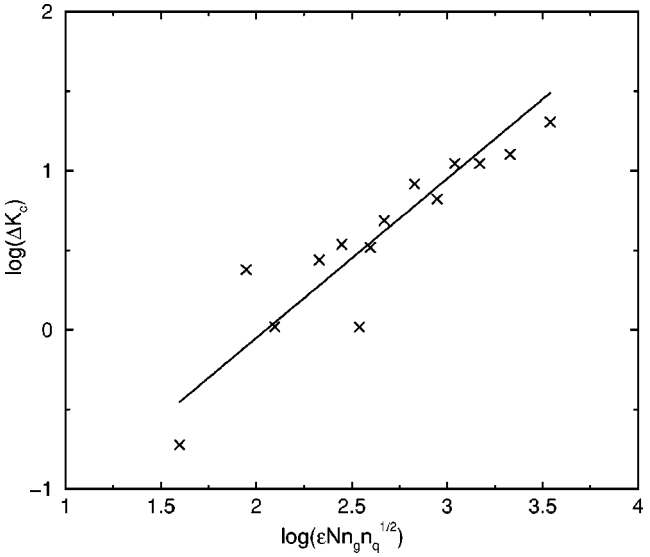

FIG. 22. Shift of the transition point due to imperfections as a function of imperfection strength and n_q. Parameters values are the same as in Fig. 21, with averages made over up to 10 realizations of disorder. Solid line corresponds to the dependence $\Delta K_c \propto \varepsilon n_g \sqrt{n_q} N$. Logarithms are decimal.

and delocalized states. In systems such as the Anderson model investigated in [30], the transition point is well defined, since all states are localized or delocalized on one side of the transition. In the case of the kicked Harper model there is some arbitrariness in the definition. We chose as transition point the value K_c (at L fixed) for which the IPR is $N_H/4=N/8$ (even for a totally delocalized state, the IPR is actually often $N_H/2=N/4$ instead of N_H due to fluctuations). In the partially delocalized regime, the IPR at fixed K should grow with ε. If the system is in the Breit-Wigner (golden rule) regime, the IPR should grow as Γ/Δ_n where $\Delta_n \sim 1/N$ is the mean level spacing and $\Gamma \approx 2\pi |V_{typ}|^2/\Delta_c \sim \varepsilon^2 n_g^2 n_q$. We therefore expect the transition point to move with imperfections as $\Gamma/\Delta_n \sim \varepsilon^2 n_g^2 n_q N$. On the contrary, in the Gaussian regime, the IPR grows like σ/Δ_n, where $\sigma \sim \varepsilon n_g \sqrt{n_q}$. In this case the transition point should move as $\varepsilon n_g \sqrt{n_q} N$.

Figure 22 shows the data numerically obtained for the shift of the transition point due to imperfections. It indicates that $\Delta K_c \sim \varepsilon n_g \sqrt{n_q} N$ agrees with the data, whereas $\varepsilon^2 n_g^2 n_q N$ is a much less reasonable scaling variable (data not shown). The data therefore seem to indicate that in the partially delocalized regime as in the localized regime, the IPR grows as $\varepsilon n_g \sqrt{n_q} N$, as does the shift of the transition point. This result is in sharp contrast with the findings of [30] for the Anderson transition, which was shown to scale polynomially with the number of qubits. In our case, the presence of delocalized state coexisting with localized states makes the delocalization much easier in presence of imperfections.

Figure 23 shows the scaling of the IPR as a function of ε. For small values of n_q, the IPR without imperfections is already a large fraction of Hilbert space dimension, so data are meaningful only for $n_r \geqslant 9$. Still, data shown in Fig. 23 seem to indicate that the regime where $\xi \propto \varepsilon$ is present, confirming that the system is in a Gaussian regime rather than in the golden rule regime.

The scaling laws obtained in this regime show that there is an exponentially small value ε_c given by Eq. (12) above which imperfections destroy the localization properties of the system. In particular, the transition point is exponentially sensitive to the number of qubits. This sharp difference between localized and delocalized regime can be easily seen on experiments: the long-time behavior of the system will be very different in both cases. Still, the algorithms presented can be useful in delocalized regime in presence of imperfections, even for $\varepsilon > \varepsilon_c$. Indeed, the system should remain close to the exact one up to a time $\sim 1/\sigma \sim 1/(\varepsilon n_g \sqrt{n_q})$ as in the localized regime, so measurability of physical quantities

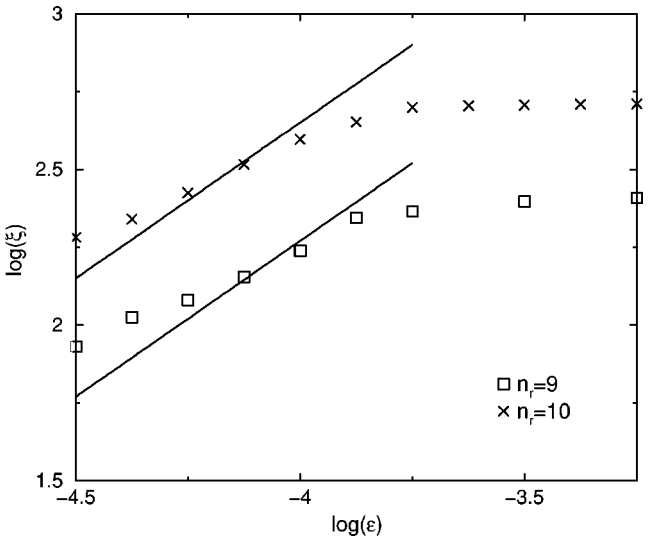

FIG. 23. IPR as a function of ε for $K=10$, $L=27$ with other parameter values the same as in Fig. 18. Solid lines correspond to the dependence $\xi \propto \varepsilon$. Logarithms are decimal.

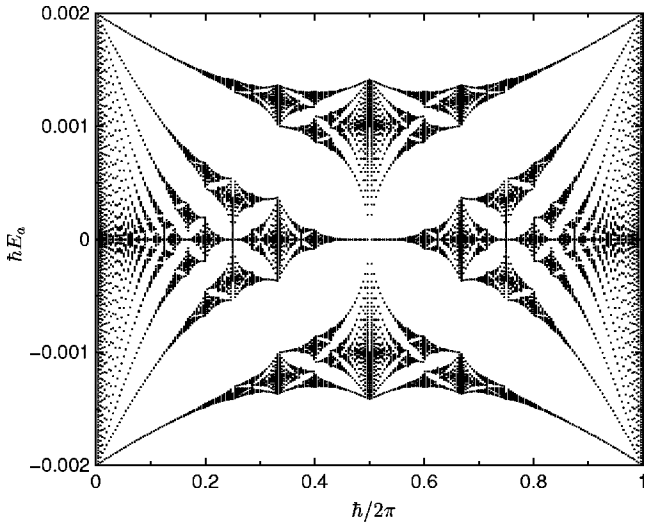

FIG. 24. Eigenphases of the Harper operator (4) as a function of $\hbar$ for $K=L=10^{-3}$; $n_r=8$.

will eventually rest on the comparison of this time scale with the time for the system to show the delocalization plateau. On the contrary, in the localized regime for moderate levels of imperfections the localization length can be measured for very long times.

V. SPECTRUM: MEASUREMENT AND IMPERFECTION EFFECTS

Another type of physical properties which can be obtained through quantum simulation of the kicked Harper model concerns the spectrum of the evolution operator $\hat{U}$. This spectrum has been the focus of many studies (see, e.g., [23]): it shows multifractal properties, and transport properties (localized or delocalized states) are reflected in the eigenvalues, as well as dynamical properties (chaotic or integrable states). Additionally, for small $K=L$, this spectrum will be close to the famous spectrum of the Harper model ("Hofstadter butterfly"), which shows fractal properties [15], as can be seen in Fig. 24.

To get information about eigenvalues, we can use the phase estimation algorithm. This algorithm, at the heart of the Shor algorithm, proceeds by transforming the state $\Sigma_t|t\rangle|\psi_0\rangle$ into $\Sigma_t|t\rangle|U^t\psi_0\rangle$. Then a QFT of the first register will give peaks at the values of the eigenphases of U. To be efficient, this process should be applied to operators U for which exponentially large iterates can be obtained in polynomial number of operations. In [45] it was suggested that even if this condition is not fulfilled one can obtain approximate eigenvalues exponentially fast provided one starts from an initial state $|\psi_0\rangle$ already close to an eigenvector. In the case at hand, we do not know how to get exponentially large iterates in polynomial time or how to build a good approximation of the eigenvectors without knowing them. We therefore suggest a third strategy, which is more generally applicable than the ones above, but does not yield an exponential gain.

We first build the state $\Sigma_{t=0}^{N_H-1}|t\rangle|\psi_0\rangle$, where $|\psi_0\rangle$ is an arbitrary quantum state on a Hilbert space of dimension $N_H=2^{n_r}$ which can be efficiently built; for example, it can be the state $2^{-n_r/2}\Sigma_n|n\rangle$, which can be obtained from $|0\rangle$ with n_r Hadamard gates. Once the state $|0\rangle|\psi_0\rangle$ is realized, it can be transformed with n_r Hadamard gates on the first register into $2^{-n_r/2}\Sigma_{t=0}^{N_H-1}|t\rangle|\psi_0\rangle$. We have seen that the evolution operator U can be implemented in poly $(\log N_H)$ operations by the three strategies exposed in Sec. III. Therefore we can apply powers of U on the second register controlled by the value of the first register. This yields $2^{-n_r/2}\Sigma_t|t\rangle|U^t\psi_0\rangle$ in $O(N_H)$ operations, up to logarithmic factors. A QFT of the first register will yield peaks centered at eigenvalues of the operator U. Thus measurement of the first register will give an eigenvalue of U with good probability in $O(N_H)$ operations including measurement. A drawback of this approach is that peaks have additional probabilities on nearby locations, and since the number of eigenvalues is N_H, measuring the precise shape of all peaks will be inefficient [$O(N_H^2)$ operations]. A more precise, although slower, method is to use amplitude amplification [46] (a method derived from the Grover algorithm [3]) to zoom on a small part of the spectrum. This enables to get the precise values of all eigenvalues in a given interval. The total cost will be $O(N_H\sqrt{N_H})$ operations. This methods which uses Grover's search on phase estimation can be seen as a process reverse to quantum counting [47] (where phase estimation is used on the Grover operator).

Calculating the spectrum by direct diagonalization of a $N_H\times N_H$ matrix such as the one of the operator $\hat{U}$ of Eq. (4) requires in general of the order of N_H^3 classical operations. However, in the case of the operator $\hat{U}$ of Eq. (4) there is a faster classical method similar to the quantum phase estimation algorithm: one iteration of $\hat{U}$ can be computed classically in $O(N_H)$ operations (up to logarithmic factors) by using the classical FFT algorithm to shift between n and θ representations and multiplying by the relevant phase in each representation. Iterating this process N_H times and keeping each intermediate wave function costs $O(N_H^2)$ operations. Then a FFT enables to get the spectrum of U with $O(N_H \log N_H)$ operations. This method was advocated in [48] for getting the spectrum of the kicked Harper model. Therefore it is possible to get the spectrum classically in $O(N_H^2)$ operations up to logarithmic factors. Thus the quantum algorithms explained above [$O(N_H)$ operations for one eigenvalue with unknown precision, $O(N_H\sqrt{N_H})$ for all eigenvalues in a given small interval] realize a polynomial gain compared to the classical ones. It is important to note that although the number of operations needed is only polynomially better in the quantum case, the spatial resources are exponentially smaller (logarithmic number of qubits compared to the number of classical bits).

The Figs. 25–27 show the spectrum of the kicked Harper model in presence of errors for both slice and Chebyshev methods. The error model chosen is the static imperfection Hamiltonian (6) as in the preceding section. The evolution operator was computed by evolving basis states in presence of errors and then diagonalizing the resulting operator. The spectrum shown corresponds to small $K=L$, where the spectrum is close to the "Hofstadter butterfly," as can be seen in Fig. 24. Only 16 eigenvalues are shown. Overall phase shifts

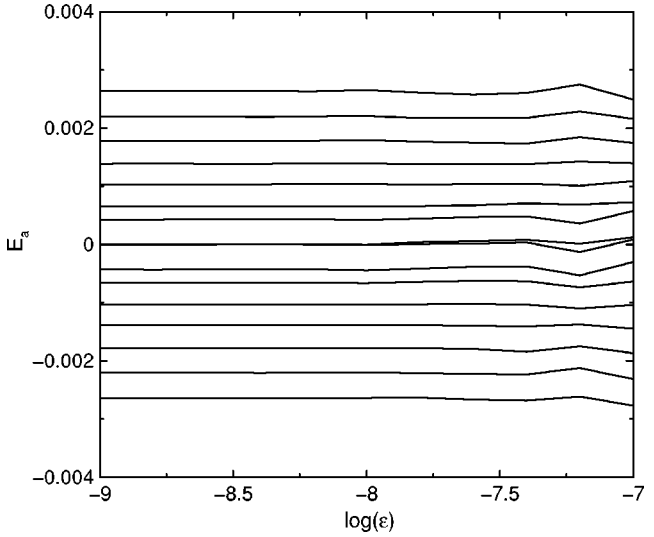

FIG. 25. Eigenphases of the evolution operator $\hat{U}$ of Eq. (4) as a function of imperfection strength. The slice method is used with 2×100 slices to compute the operator. The 16 eigenphases closest to 0 are shown. Here $n_r=6$ ($n_q=n_r+1$), $\hbar=2\pi/2^6$ (actual value is the nearest fraction with denominator 2^6), and $K=L=10^{-3}$. An overall phase factor (global motion of eigenvalues) has been eliminated. Logarithm is decimal.

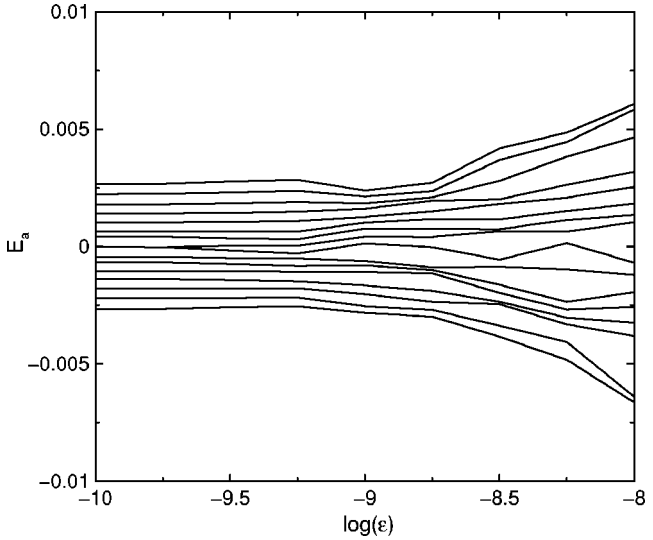

FIG. 27. Eigenphases of the evolution operator $\hat{U}$ of Eq. (4) as a function of imperfection strength. The Chebyshev method is used; a Chebyshev polynomial of degree 6 is taken, keeping all gates. The 16 eigenphases closest to 0 are shown. Here $n_r=6$ ($n_q=n_r$), $\hbar=2\pi/2^6$ (actual value is the nearest fraction with denominator 2^6), and $K=L=10^{-3}$. An overall phase factor (global motion of eigenvalues) has been eliminated. Logarithm is decimal.

due to errors were eliminated since it seems reasonable they can be estimated and compensated. It is clear from the data presented that eigenvalues are much more sensitive to strength of errors than transport properties. Numerical limitations prevented us to find the scaling in n_q of error effects, but Figs. 26–28 show the scaling with respect to ε at constant n_q.

In the case of the slice method, the average error on the eigenvalue is clearly linear in ε. We think this corresponds probably to a perturbative regime, since small values of ε are involved. For the Chebyshev method, our data indicate that a lower level of errors is needed than in the slice method to get good accuracy. This could have been expected, since we established in Sec. III that this method necessitates more gates for a similar accuracy, and each gate introduces errors. The scaling of errors with respect to ε indicates the law $\Delta E \sim \varepsilon^{\alpha}$ with $\alpha \approx 1.3$.

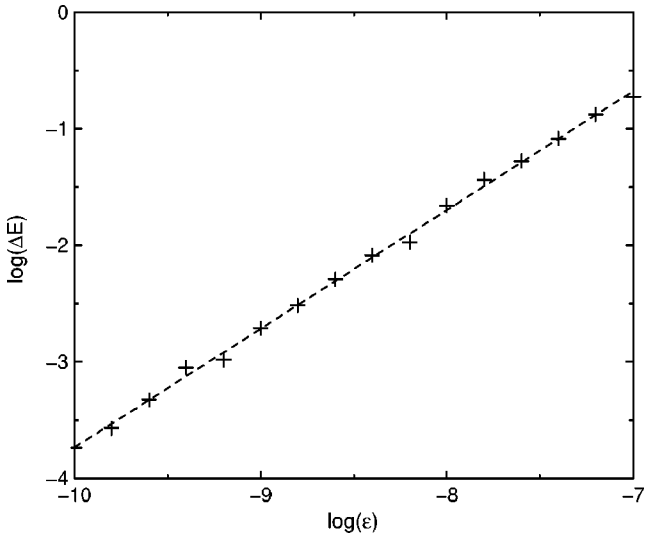

FIG. 26. Average error (in units of mean level spacing) of computed eigenphases through the slice method as a function of imperfection strength; parameters are the same as in Fig. 25, and averages were made over all eigenvalues and over 10 realizations of disorder. Dashed line corresponds to $\Delta E \propto \varepsilon$. Logarithms are decimal.

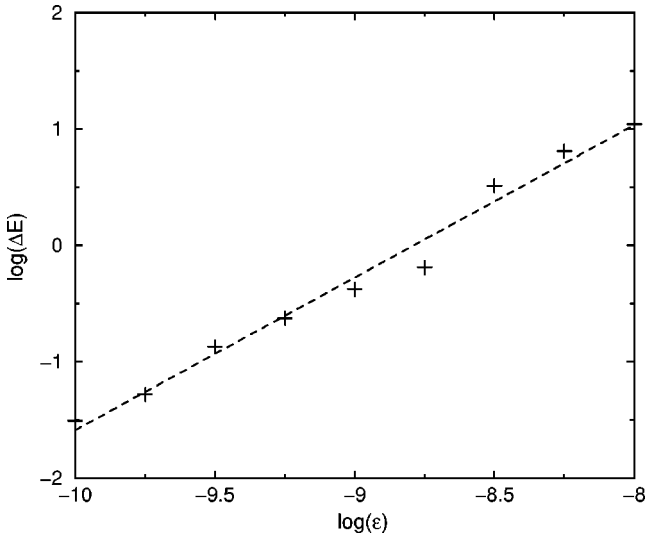

FIG. 28. Average error (in units of mean level spacing) of computed eigenphases through the Chebyshev method as a function of imperfection strength; parameters are the same as in Fig. 27, and averages were made over all eigenvalues. Dashed line corresponds to $\Delta E \propto \varepsilon^{1.3}$. Logarithms are decimal.

VI. CONCLUSION

In this paper, several quantum algorithms were presented which enable to simulate the quantum kicked Harper model, a complex system with relevance to certain physical problems. The comparison showed that while the slice method and the Chebyshev method are approximate, they are much more economical in resources than the exact simulation. It was also shown that different transport and spectral properties can be obtained more efficiently on a quantum computer than classically, although the gain is only polynomial. Numerical simulations enabled us to precise the effect of numerical errors on these algorithms and also to evaluate the effects of imperfections. The results show that depending on the regime of parameters, the same quantity can be stable or exponentially sensitive to imperfections. In general, in presence of moderate amount of errors the results of the algorithm can be meaningful, but a careful choice of the measured quantities should be done. For the different quantities computed, the slice method was shown to be more efficient and resilient to errors than the Chebyshev method, although the latter is similar to the method used in classical computers to evaluate functions.

Our results show that interesting quantum effects such as fractal-like spectrum, localization properties, and anomalous diffusion are already visible with $7-8$ qubits. We therefore believe that such algorithms could be used in experimental implementations in the near future.

ACKNOWLEDGMENTS

We warmly thank Dima Shepelyansky for many helpful suggestions in the course of this work and also Andrei Pomeransky and Klaus Frahm for several discussions. We thank the IDRIS in Orsay and CalMiP in Toulouse for access to their supercomputers. This work was supported in part by the NSA and ARDA under ARO Contract No. DAAD19-01-1-0553, by EC RTN Contract No. HPRN-CT-2000-0156, and by project EDIQIP of the IST-FET program of the EC.

[1] M. A. Nielsen and I. L. Chuang, *Quantum Computation and Quantum Information* (Cambridge University Press, Cambridge, England, 2000).
[2] P. W. Shor, in *Proceedings of the 35th Annual Symposium on the Foundations of Computer Science*, edited by S. Goldwasser (IEEE Computer Society, Los Alamitos, CA, 1994), p. 124.
[3] L. K. Grover, Phys. Rev. Lett. **79**, 325 (1997).
[4] S. Lloyd, Science **273**, 1073 (1996); D. S. Abrams and S. Lloyd, Phys. Rev. Lett. **79**, 2586 (1997).
[5] D. A. Lidar and O. Biham, Phys. Rev. E **56**, 3661 (1997); A. Sørensen and K. Mølmer, Phys. Rev. Lett. **83**, 2274 (1999).
[6] B. Georgeot and D. L. Shepelyansky, Phys. Rev. Lett. **86**, 5393 (2001).
[7] B. Georgeot, Phys. Rev. A **69**, 032301 (2004).
[8] R. Schack, Phys. Rev. A **57**, 1634 (1998).
[9] Y. S. Weinstein, S. Lloyd, J. Emerson, and D. G. Cory, Phys. Rev. Lett. **89**, 157902 (2002).
[10] B. Georgeot and D. L. Shepelyansky, Phys. Rev. Lett. **86**, 2890 (2001).
[11] B. Lévi, B. Georgeot, and D. L. Shepelyansky, Phys. Rev. E **67**, 046220 (2003).
[12] G. Benenti, G. Casati, S. Montangero, and D. L. Shepelyansky, Phys. Rev. Lett. **87**, 227901 (2001).
[13] K. M. Frahm, R. Fleckinger, and D. L. Shepelyansky, Eur. Phys. J. D **29**, 139 (2004).
[14] P. G. Harper, Proc. Phys. Soc., London, Sect. A **68**, 874 (1955).
[15] D. R. Hofstadter Phys. Rev. B **14**, 2239 (1976).
[16] A. Barelli, J. Bellissard, and R. Rammal, J. Phys. (Paris) **51**, 2167 (1990); A. Barelli and C. Kreft, J. Phys. I **1**, 1229 (1991).
[17] T. Geisel, R. Ketzmerick, and G. Petschel, Phys. Rev. Lett. **66**, 1651 (1991).
[18] M. Wilkinson and R. J. Kay Phys. Rev. Lett. **76**, 1896 (1996).
[19] S. N. Evangelou and J.-L. Pichard, Phys. Rev. Lett. **84**, 1643 (2000).
[20] P. Leboeuf, J. Kurchan, M. Feingold, and D. P. Arovas, Phys. Rev. Lett. **65**, 3076 (1990).
[21] R. Lima and D. L. Shepelyansky, Phys. Rev. Lett. **67**, 1377 (1991).
[22] R. Artuso, G. Casati, and D. L. Shepelyansky, Phys. Rev. Lett. **68**, 3826 (1992).
[23] R. Artuso, F. Borgonovi, I. Guarneri, L. Rebuzzini, and G. Casati, Phys. Rev. Lett. **69**, 3302 (1992); R. Artuso, G. Casati, F. Borgonovi, L. Rebuzzini, and I. Guarneri, Int. J. Mod. Phys. B **8**, 207 (1994).
[24] I. Dana, Phys. Rev. Lett. **73**, 1609 (1994).
[25] F. Borgonovi, and D. L. Shepelyansky, Europhys. Lett. **29** (2), 117 (1995).
[26] R. Ketzmerick, K. Kruse, and T. Geisel, Phys. Rev. Lett. **80**, 137 (1998).
[27] T. Prosen, I. I. Satija, and N. Shah, Phys. Rev. Lett. **87**, 066601 (2001).
[28] P. Leboeuf and A. Mouchet, Phys. Rev. Lett. **73**, 1360 (1994).
[29] O. Brodier, P. Schlagheck, and D. Ullmo, Phys. Rev. Lett. **87**, 064101 (2001).
[30] A. A. Pomeransky and D. L. Shepelyansky, Phys. Rev. A **69**, 014302 (2004).
[31] V. V. Dobrovitski, H. A. De Raedt, M. I. Katsnelson, and B. N. Harmon, Phys. Rev. Lett. **90**, 210401 (2003).
[32] J. P. Paz, A. J. Roncaglia, and M. Saraceno, Phys. Rev. A **69**, 032312 (2004).
[33] D. Jaksch and P. Zoller, New J. Phys. **5**, 56 (2003).
[34] J. Stoer and R. Bulirsch, *Introduction to Numerical Analysis* (Springer-Verlag, New York, 1993).
[35] B. Georgeot and D. L. Shepelyansky, Phys. Rev. E **62**, 3504 (2000); **62**, 6366 (2000).
[36] M. Terraneo and D. L. Shepelyansky, Phys. Rev. Lett. **90**, 257902 (2003).
[37] E. Wigner, Phys. Rev. **40**, 749 (1932); M. V. Berry, Philos. Trans. R. Soc. London, Ser. A **287**, 237 (1977).
[38] C. Miquel, J. P. Paz, and M. Saraceno Phys. Rev. A **65**,

062309 (2002).
[39] S.-J. Chang and K.-J. Shi, Phys. Rev. A **34**, 7 (1986).
[40] C. Miquel, J. P. Paz, M. Saraceno, E. Knill, R. Laflamme, and C. Negrevergne, Nature (London) **418**, 59 (2002).
[41] G. Benenti, G. Casati, S. Montangero, and D. L. Shepelyansky, Phys. Rev. A **67**, 052312 (2003); G. Benenti, G. Casati, and S. Montangero, Quantum Inf. Process. **3**, 53 (2004).
[42] B. Georgeot and D. L. Shepelyansky, Phys. Rev. Lett. **79**, 4365 (1997); V. V. Flambaum and F. M. Izrailev, Phys. Rev. E **56**, 5144 (1997).
[43] G. Benenti, G. Casati, S. Montangero, and D. L. Shepelyansky, Eur. Phys. J. D **20**, 293 (2002).
[44] O. P. Sushkov and V. V. Flambaum, Sov. Phys. Usp. **25**, 1 (1982).
[45] D. S. Abrams and S. Lloyd Phys. Rev. Lett. **83**, 5162 (1999).
[46] G. Brassard and P. Høyer, in *Proceedings of Fifth Israeli Symposium on Theory of Computing and Systems* (IEEE Computer Society, Los Alamitos, CA, 1997), pp. 12–23; G. Brassard, P. Høyer, M. Mosca, and A. Tapp, in *Quantum Computation and Quantum Information: A Millennium Volume*, edited by S. J. Lomonaco, Jr. and H. E. Brandt (AMS, Contemporary Mathematics Series Vol. 305, 2002).
[47] M. Boyer, G. Brassard, P. Høyer, and A. Tapp, Fortschr. Phys. **46**, 493 (1998).
[48] R. Ketzmerick, K. Kruse, and T. Geisel, Physica D **131**, 247 (1999).